EXPERIMENTAL STUDY OF WAKES AND VORTICES FOR A FLOW PAST A CIRCULAR CYLINDER AT LOW REYNOLDS NUMBER

Thesis (Major Project – II ME499)

Submitted in partial fulfillment of the requirements for the degree of

BACHELOR OF TECHNOLOGY

in

MECHANICAL ENGINEERING

by

MOOL CHANDRA (12ME85)

PRASHANTH RAMESH (12ME101)

SANDEEP MOUDGALYA (12ME113)

SOMESH BHATIA (12ME131)

**DEPARTMENT OF MECHANICAL ENGINEERING
NATIONAL INSTITUTE OF TECHNOLOGY
KARNATAKA, SURATHKAL MANGALORE – 575025
MAY 2016**

DECLARATION

By the B.Tech. Students

We hereby declare that the Project Work Report entitled

EXPERIMENTAL STUDY OF WAKES AND VORTICES FOR A

FLOW PAST A CIRCULAR CYLINDER AT LOW REYNOLDS

NUMBER

which is being submitted to the National Institute of Technology Karnataka, Surathkal for the award of the Degree of Bachelor of Technology in Mechanical Engineering is a bonafide report of the work carried out by us. The material contained in this Project Work Report has not been submitted to any University or Institution for the award of any degree.

Register Number, Name & Signature of the Student(s):

1. 12ME85 – Mool Chandra

2. 12ME101 – Prashanth Ramesh

3. 12ME113 – Sandeep R Moudgalya

4. 12ME131 – Somesh Bhatia

Department of Mechanical Engineering

Place: NITK - SURATHKAL

Date:

CERTIFICATE

This is to certify that the B.Tech Project Work Report entitled

EXPERIMENTAL STUDY OF WAKES AND VORTICES FOR A FLOW

PAST A CIRCULAR CYLINDER AT LOW REYNOLDS NUMBER

is submitted by:

	Roll no	Name	Signature
1.	12ME85	Moolchandra	
2.	12ME101	Prashanth Ramesh	
3.	12ME113	Sandeep R Moudgalya	
4.	12ME131	Somesh Bhatia	

As a record of the work carried out by them, is accepted as the B.Tech. Project Work Report submission in partial fulfilment of the requirements for the award of degree of Bachelor of Technology in Mechanical Engineering.

Dr. Ravikiran Kadoli

Guide

Dr. Vijay Desai

Chairman-DUGC

A C K N O W L E D G E M E N T

Abstract

The aim of the project is to perform the experimental study of the wakes and vortices for a flow past a circular cylinder at low Reynolds number. To design the experimental test section a review of literature was performed to come up with the suitable dimensions for the experimental test section. Calculations were performed to obtain the power required to drive the flow in the channel, thus the pump was selected. Also, both 2D and 3D drawings of the test section were prepared using AutoCAD and CATIA respectively. The 3D drawings consist of both assembled drawings and part drawings to enable better understanding and ease of assembly of test section. The components required were procured after obtaining approval from the department. Thereafter, the fabrication of the test section was performed. Once the test section was fabricated the system was checked for leaks and then assembled. The assembled setup was then used to perform the flow visualisation around a cylinder. The experiments showed various wake patterns at differing speed ranges. The flow was visualised using different coloured inks. The images were captured using a DSLR camera with appropriate background lighting. The flow rate at which the experiments were conducted was measured. The images captured during the flow visualization experiments were found to be in good agreement with the flow patterns available in the literature for the given speed ranges.

In addition to this, attempt using finite difference method was made to develop a Navier Stokes solver. A code using an explicit scheme for the Lid driven cavity test case and the results were validated with the benchmark results of Ghia et al. (1982). Further, the code was extended to obtain the flow solution for a flow past a square cylinder.

Contents

List of Figures

Nomenclature

u	Velocity in X direction
v	Velocity in Y direction
ρ	Density of fluid
t	Time
p	Pressure
Δx	Grid spacing in X
Δy	Grid spacing in Y
Δt	Increment in time
n	Representation of time step
Re	Reynolds number
ν	Kinematic viscosity
d	Diameter of cylinder
μ	Dynamic viscosity
Q	Volumetric flow rate
A	Area of crossection

Chapter 1

Introduction

1.1 Flow across bluff bodies

In spite of extensive numerical and experimental studies for over a century, flow across bluff bodies have been of great engineering significance and a subject of interest but understanding flow behind a bluff body poses a great challenge. In the beginning of the 20th century during the study of flows, physicists believed that viscosity does not play a part in the flow. This predicted the drag to be zero on a body subjected to steady flow which is a discrepancy and was known as d'Alembert's paradox. This paradox was resolved by Ludwig Prandtl who showed that viscous effects can never be neglected. The viscous effects are not confined to a thin layer which can be observed in cases such as flow past a bluff body like a sphere. Thus Prandtl gave rise to the concept of boundary layers (Goldstein, 1969).

The idea of flow past bluff bodies is not just limited to the design of aircrafts, automobiles and buildings. It can also be noticed in cases such as sports aerodynamics wherein the study is used to optimize the performance of athletes, another example could be the design of a football which is a demonstration of flow past a rotating sphere. Some of the examples that are quoted above may not have been amongst the motivating factors for earlier researchers who studied this field but these factors are relevant in the present scenario.

Bluff body wakes are complex due to interaction of boundary layer, a separating free shear layer, and a wake (Williamson, 1996). Flow past a circular cylinder produces

1

boundary layer separation at upper and lower portion of the cylinder. This leads to an onset of instability of the wake flow beyond a critical Reynolds number which causes alternating shedding of vortices, well-known in literature as von Karman Vortex Street. The "singing" of telephone and transmission lines has been attributed to this phenomenon.

Vortex-induced vibrations (VIV) are caused by fluid structure interaction between a bluff body and an external flow. They can cause vibration of heat exchanger tubes, alter the dynamics of civil engineering structures like bridges, chimneys and offshore oil riser tubes. VIV can cause large-amplitude vibrations of tethered structures in the ocean and can cause damage due to fatigue (Williamson and Govardhan, 2004).

1.2 Experimental Fluid Mechanics

Though the study of fluid mechanics is extremely challenging and complex, discovering ways in which fluids behave and react is rewarding. These results have helped in verifying CFD predictions. Water tunnel has been extensively used for testing the hydrodynamic behaviour of submerged body in flowing water. Wind tunnel, instrumented with suitable sensors is used to measure aerodynamic forces, pressure distribution, or other aerodynamic-related characteristics. Flow visualisation has been extensively used to make the flow patterns visible in order to get qualitative or quantitative information of them. Flow can be visualised by three methods: surface flow visualisation, particle tracer methods and optical methods. The above techniques of measurements can provide whole, instantaneous fields of scalars and vectors (Adrian, 1991).

1.3 Computational fluid dynamics

Computational fluid dynamics (CFD) is a branch of fluid mechanics that uses numerical analysis and algorithms to solve fluid flow problems. Computers are used to perform the calculations required to simulate the interaction of liquids and gases with surfaces defined by boundary conditions. This technique is very powerful and it spans a wide range of industrial and non-industrial applications. Some examples are: aerodynamics of aircraft, hydrodynamics of ship, turbo machinery, chemical process engineering and cooling of electronic equipment. CFD offers several unique advantages towards fluid systems design: substantial reduction in lead time and costs of new designs, ability to study systems where controlled experiments are difficult or impossible to perform and the ability to study systems under hazardous conditions.

1.4 Examples of flow past bluff bodies

1.4.1. Golf Ball Aerodynamics

In the early days of the sport, golf balls were made with a smooth surface. It was soon realized, however, that when the surface became worn the ball travelled farther when driven, and subsequently golf balls were manufactured with a dimpled surface to simulate the worn surface. As shown in Figure 1.1, the air flow around the smooth ball is laminar and that around the dimpled golf ball is turbulent. The reason for the increase in driven distance with the rough surface is that the rough surface promotes early transition due to which the critical Reynolds number may be low and this gives a critical speed for a golf ball well below the flight speed. Thus, with the roughened surface, the ball travels at above the critical drag speed during its flight and

so experiences a smaller decelerating force throughout, with consequent increase in range.

Smooth

ball

Air quickly separates from ball.

Golf ball

Turbulence sucks air to ball. Separation is delayed.
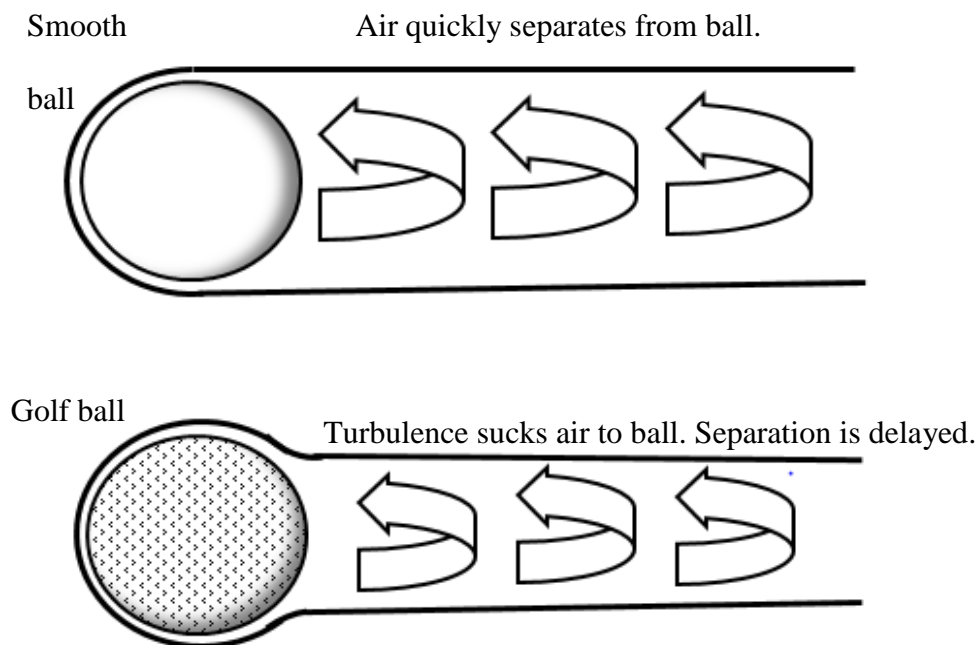
Figure 1.1 - Golf ball aerodynamics showing delayed separation in a dimpled surface.

1.4.2. Magnus Effect

Magnus effect, generation of a sidewise force on a spinning cylindrical or spherical solid immersed in a fluid (liquid or gas) when there is relative motion between the spinning body and the fluid. Named after the German physicist and chemist H.G. Magnus, who first (1853) experimentally investigated the effect, it is responsible for the "curve" of a served tennis ball or a driven golf ball and affects the trajectory of a spinning artillery shell.

A spinning object moving through a fluid departs from its straight path because of pressure differences that develop in the fluid as a result of velocity changes induced

4

by the spinning body. The Magnus effect is a particular manifestation of Bernoulli's theorem: fluid pressure decreases at points where the speed of the fluid increases. In the case of a ball spinning through the air, the turning ball drags some of the air around with it (Figure 1.2). Viewed from the position of the ball, the air is rushing by on all sides. The drag of the side of the ball turning into the air (into the direction the ball is traveling) retards the airflow, whereas on the other side the drag speeds up the airflow. Greater pressure on the side where the airflow is slowed down forces the ball in the direction of the low-pressure region on the opposite side, where a relative increase in airflow occurs.
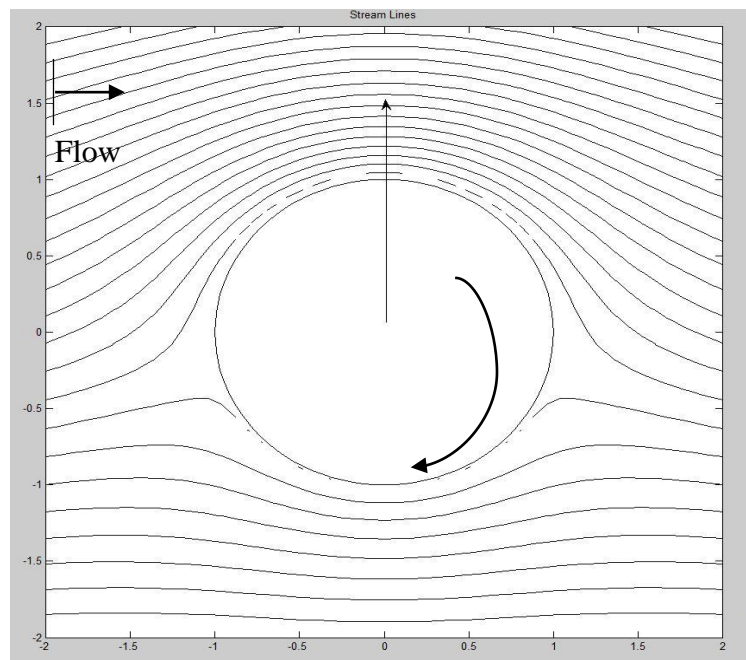
Figure 1.2 - Magnus effect.

1.4.3. Fish Propulsion

Fish swim by exerting force against the surrounding water. There are exceptions, but this is normally achieved by the fish contracting muscles on either side

5

of its body in order to generate waves that travel the length of the body from nose to tail, generally getting larger as they go along. The tail has a cross section resembling that of a symmetric aerofoil (Figure 1.3). The sequence 1 to 5 represents the positions of the tail during the tail's motion to the left. A quick change of orientation occurs at one extreme position of the oscillation during 1 to 2; the tail then moves to the left during 2 to 4, and another quick change of orientation occurs at the other extreme during 4 to 5. The vector forces exerted on the water by such motion cancel out laterally, but generate a net force backwards which in turn pushes the fish forward through the water.
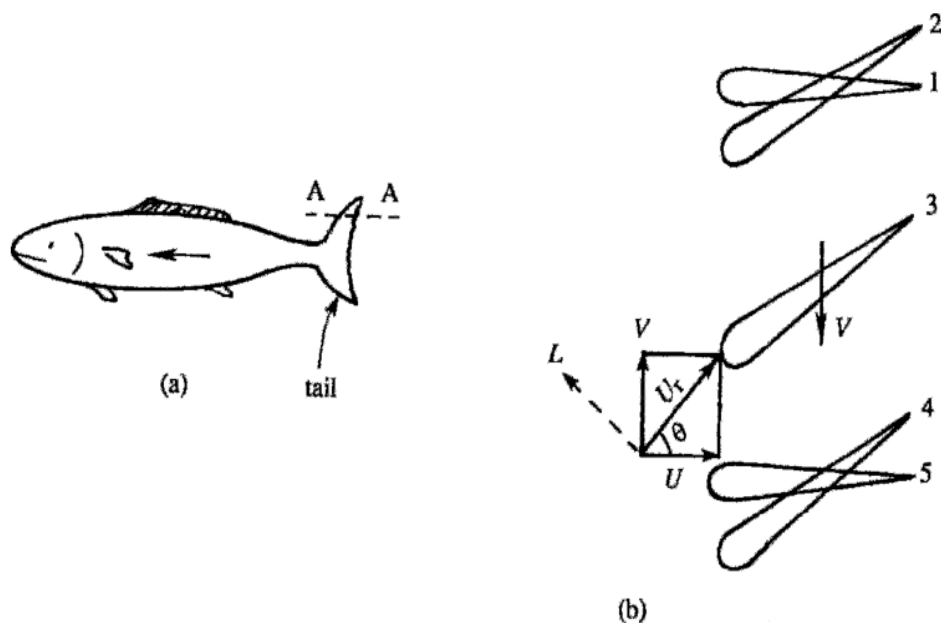
Figure 1.3 - Propulsion of fish. (a) Cross section of the tail along AA is a symmetric aerofoil. Five positions of the tail during its motion to the left are shown in (b). The lift force L is normal to the resultant speed Ur of water with respect to the tail. (Figure taken from Kundu and Cohen, 2008).

1.4.4. Boundary Layer Control

In the case of a free stream flow past a cylinder, a number of methods may be employed to control the boundary layer separation that occurs due to the adverse pressure gradient. Rotation of the cylinder can reduce or eliminate the boundary layer that is formed on the side which is moving in the same direction as the free stream. The side moving against the flow also exhibits only partial separation of the boundary layer. Suction applied through a slit in the cylinder near a separation point can also delay the onset of separation by removing fluid particles that have been slowed in the boundary layer. Alternatively, fluid can be blown from a faired slit such that the slowed fluid is accelerated and thus the point of separation is delayed.

Chapter 2

Literature Survey

Initial experiments on two-dimensional flow past a circular cylinders was performed in Cavendish laboratory, Cambridge where drag was measured by observing the bending of glass fibres in a wind tunnel (Tritton, 1959). Comparisons were made with other experimental values and with various theoretical calculations.

The principal features of an experimental investigation of the steady separated flow past a circular cylinder in the Reynolds number range of about 30 to 300 was determined by Grove, Shair, Shair and Petersen (1964). This system was studied up to Reynolds numbers considerably larger than any previously attained, thus providing a much clearer insight into the asymptotic character of such flows at high Reynolds numbers. It was found that the pressure coefficient at the rear of the cylinder remained unchanged for $25 < R < 177$, that the circulation velocity within the wake approached a non-zero limit as the Reynolds number increased, and that the wake length increased in direct proportion to the Reynolds number. All of the above were determined with the aid of an oil tunnel, manometer and a cathetometer.

Son and Hanratty (1968) in their work attempted to find the steady flow solution for the flow around a cylinder at Reynolds numbers 40,200 and 500. The motivation was to obtain the steady flow solution at Reynolds number tending to infinity. The formulation was carried out using Finite difference method with polar grids with finer mesh size close to the cylinder. The mathematical formulation was done using stream function φ and vorticity ω. The equations were solved using an alternating direction

implicit scheme. This formulation resulted in accurate streamline results obtained up to Reynolds number 500.

The recent interest in the fluid mechanics of dilute polymer solutions has been motivated by a phenomenon known as the Tom's effect - the reduction of wall shear stress in a turbulent flow when minute amounts of a high molecular weight polymer is present. James and Acosta (1970) measured of heat transfer and drag for the flow of dilute polymer solutions around very small cylinders. These flow-visualization studies showed that the streamline pattern with dilute polymer solutions can be significantly different from that with Newtonian fluids because of viscoelastic effects.

Fornberg (1980) in his work attempts to perform a numerical study of steady viscous flow past a circular cylinder. He addresses problems related to numerical difficulties involved in simulating flow at high Reynolds numbers. The mathematical formulation is done in terms of stream function φ and vorticity ω. The flow field is taken as symmetric about the central plane and the equations are solved after transforming the coordinate system to polar. The vorticity equation is elliptic in nature for steady equations and are solved using the successive over relaxation technique. The treatment of boundary conditions is done based on the Reynolds number of the flow. The solution procedure involves guessing the values of φ and ω, then obtain improvements by performing one iteration on the inner grid and solving Poisson equation for the outer grid. The results were obtained for Reynolds numbers up to 260.

Saffman and Schatzman (1982) developed an invisid model for the Karman vortex street. It contained vortices of uniform vorticity surrounded by irrotational fluid. This was related to the wake behind a bluff body by a global analysis requiring the

conservation of momentum, energy and vorticity. A qualitative procedure was proposed whereby the slow evolution of the wake through viscous effects was approximated. Some calculations were made for the 'secondary vortex street' that was observed after breakdown and rearrangement, and corresponding comparison were made with experiment.

Gharib and Derango (1989) developed an experimental approach to study two-dimensional flow phenomena using a soap film which is capable of producing purely two-dimensional flows. In this new technique, a suspended liquid film (a soap film) is set in motion in a long frame using a planar water jet as a pulling mechanism. By producing film velocities up to 250 cm/s, this device can generate a variety of shear flows for quantitative studies via laser Doppler velocimetry. Several examples of shear flows are presented such as flow past circular cylinder, circulating flow inside cavity and flow over a backward facing step. It is shown that this device can be a valuable tool in establishing a quantitative experimental basis for two-dimensional flows including wakes, jets, mixing layers and grid-generated turbulence.

Fundamental characteristics of the low-Reynolds-number cylinder wake is the phenomenon of oblique vortex shedding and discontinuities in the Strouhal-Reynolds number relationship. Paper shows that both of these characteristics of the wake are directly related to each other, and that both are influenced by the boundary conditions at the ends of the cylinder. Flow between Reynolds numbers of 49 to 178 was studied. Measurements of velocity fluctuations were made with a miniature hot wire situated in the wake of three different cylinders (of diameters 0.051, 0.061, 0.104 cm.) in a 6 in. diameter circular test section of an open-jet wind tunnel. The Strouhal frequency

measurements were somewhat unrepeatable, the results were influenced by the end conditions of the wall boundary layers. The use of endplates dramatically improved the repeatability of the Strouhal measurements, and served as an early demonstration of the importance of the end conditions on the flow across even large spans. Two cylinders of different diameter both produce a discontinuity in the Struohal number at the same Re = 64, unlike the Re=300 as predicted earlier. The Strouhal discontinuity at Re = 64 is caused by a change from one mode of oblique vortex shedding to another oblique mode, and is not due either to non-uniform flow conditions or, as was already found, to flow induced vibrations. As Re is decreased, the oblique angle (theta) increases, until there is some form of 'breakdown' to a different mode of shedding. The needed L/D ratio for the cylinder to be free from such effects was found to be > 45, not 20 as found previously (Williamson, 1989).

Armfield in his work attempts to come up with solution using Finite Difference Methods for both staggered and non-staggered grids. The approach taken is similar to that of Rhie and Chow who came up with a numerical scheme for non-staggered grids and the scheme which mimics the features of SIMPLE. The scheme possesses integrability and is strongly elliptic in nature. The results suggest that the scheme proposed here is faster in computations in case of non-uniform meshes and also is adaptable to multi-grid techniques (Armfield, 1991).

Wesseling et al. (1991) using standard tensor notation derived a coordinate invariant finite volume discretization of incompressible Navier-Stokes equations on staggered grids in general coordinates. The steps taken were: Boundary-fitted coordinate mapping, applying Divergence Theorem, choosing the unknowns applying

11

tensor formulation, finally using finite volume discretization, time discretization and solution method it was concluded that results of satisfactory accuracy were obtained, provided $V_a = \sqrt{gU_a}$ are used as cotravariant velocity unknowns.

Norberg (1993) studied the influence of aspect ratio in flow past a circular cylinder using end plates to change the aspect ratio in a wind tunnel. The Strouhal number was measured by recording the output from standard single hot wires. The measurements with the music wires were carried out downstream of the cylinders. This study consisted of measuring the Strouhal number and the mean base suction coefficient, both measured at the mid-span position in cylinders where L/D ratio is very large. Reynolds numbers from about 50 to 4 x 10^4 were investigated. At aspect ratios larger than about 100 and for highly uniform upstream conditions, the measured Strouhal numbers (at around mid-span) were independent of the aspect ratio. In such cases, however, parallel shedding condition was only indicated at Reynolds numbers lower than about 70. For analysing turbulent flow, quasi-infinite cylinders are required to remove end effects at the mid-section. As Re increases, so does the L/D ratio needed. In the beginning of the transition regime, i.e. from $Re = 160$ to 230, aspect ratios of the order 50 were needed in order to represent the flow around a 'quasi-infinite' cylinder. At around the transition occurring at $Re = 250$, however, an aspect ratio larger than about 200 was indicated. Further: $350 < Re < 600$: L/D >=100; $600<= Re < 4000$: L/D >= 50; $4000 < Re < 104$: L/D >=60-70 and finally $104 <= Re < 4x104$: L/D >= 25. This experiment was for the most part for data collection and comparison with existing theoretical models. A good correlation was found when the necessary dimensions were taken.

The modes of vortex formation and frequency response of a freely vibrating cylinder was studied by Govardhan and Williamson (2000). They studied the transverse vortex-induced vibrations of an elastically mounted rigid cylinder in a fluid flow. Simultaneous force, displacement and vorticity measurements using digital particle image velocimetry were done for the first time in free vibrations. They found that there existed two distinct types of response in such systems, depending on whether one has a high or low combined mass-damping parameter. In the classical high mass-damping case, an `initial' and `lower' amplitude branch are separated by a discontinuous mode transition, whereas in the case of low mass-damping case, a further higher-amplitude `upper' branch of response appears, and there exist two mode transitions. To understand the existence of more than one mode transition for low two distinct formulations of the equation of motion were employed. One of which used the `total force', while the other uses the `vortex force', which is related only to the dynamics of vorticity.

Baranyi (2000) presented a finite difference solution for a 2-D, unsteady incompressible Navier-Stokes equations for laminar flow about fixed and oscillating cylinders. He used boundary-fitted coordinates and the governing equations were transformed to a non-inertial system fixed to the accelerating cylinder. Convective terms were handled by a third order modified upwind difference, other space derivatives were handle by fourth order central differences and time derivatives by forward differences. The computed Strouhal numbers and time-mean drag coefficients for fixed cylinders compared well with experimental results. Amplitude bounds of locked-in vortex shedding due to forced transverse oscillation were determined for a fixed Re number. Computations were carried out for a cylinder in orbital motion placed in a uniform flow.

The study conducted by Breuer et al. (2000) consisted of analysing the 2D flow across a square cylinder. The Lattice-Boltzmann method was the Lattice-BKG method. Finite element method consisted of Navier-Stokes solver for non-orthogonal body-fitted grids. Both methods were of second order accuracy in space and time. Results of both methods, i.e velocity profile, drag coefficient, recirculation length and Strouhal number were compared and found to match well. *Re* ranged from 0 to 300. Above 300, flow is considered 3D and cannot be analysed by this method.

Guilmineau and Queutey, in their work have come up with a numerical simulation to model the vortex shedding in case of an oscillating cylinder. They have used FVM to implement the flow solution. The PISO algorithm is used for the pressure-velocity coupling. They have performed simulations for both cross flow and transverse flow for Reynolds number up to 185 (Guilmineau and Queutey, 2002).

The analysis of two and three-dimensional flow past a circular cylinder in different laminar flow regimes is presented in this work. An implicit pressure-based finite volume method is used for time-accurate computation of incompressible flow using second order accurate convective flux discretization schemes. All the computations use an implicit pressure-based finite volume Navier–Stokes algorithm. Analysis is performed on the range of $0.1 < Re < 400$. Data is compared with existing data of the experiment from different studies. Up to Re of 200, the two-dimensional computation results agree reasonably well with the accurate measurement data. Two-dimensional flow computation has been carried out for different values of Re between 47 and 400. Beyond Re=49, where the flow becomes unsteady, gross discrepancies are observed over the range of Re between 49 and 300. At Re = 200 and 300, the

discrepancies are attributed to the three-dimensional instability of the wake. At low Reynolds number Re < 200, the discrepancies may be attributed to the blockage effect (Rajani et. al, 2009).

In an interesting attempt, Sun et al. have developed a finite volume solver for incompressible flows. They have used pressure-velocity framework on the non-staggered, unstructured grids and have modeled the flow using immersed boundary conditions. The purpose of this study is to develop flow solution at low Reynolds numbers to be used in MEMS (Micro Electro Mechanical System) based applications (Sun, Mathur and Murthy, 2010).

Coe (2011) in his work has solved the lid driven cavity flow problem using a Staggered Finite Volume Pressure correction method. The velocity at each time step is calculated as a sum of the pressure gradient from the previous time step and as an intermediate velocity. The intermediate velocity is calculated based on two computations. Firstly, Adams-Bashforth scheme is used to advance to the intermediate solution. For this, the pressure terms are neglected. The second set of computations involves solving the pressure correction equation and thus the corrected pressure values are used to update the earlier obtained intermediate velocity. The solution procedure is implemented using an alternating direction implicit solver with SOR and in conjunction with Taylor algorithm. The results were compared with the available results from literature (Ghia et. al, 1982).

Shukla and Arakeri investigated the effect of a prescribed tangential velocity on the drag force on a circular cylinder in a span wise uniform cross flow. Using a combination of theoretical and numerical techniques the optimal tangential velocity

profiles which will reduce the drag force acting on the cylindrical body is determined. Pressure is determined through a straightforward integration of the θ component of the Navier–Stokes equations. Drag is computed by considering its dependency only on the first harmonic of the far field pressure. It is observed that the computed results are in good agreement with those reported in previous studies for a cylinder with a stationary and a perfect slip boundary at various Reynolds numbers (Shukla and Arakeri, 2013).

Gonçalves et al. (2015) performed experiments on the flow around stationary circular cylinders with very low aspect ratio piercing the water free surface were carried out in a recirculating water channel. Eight different aspect ratios were tested, namely L/D= 0.1, 0.2, 0.3, 0.5, 0.75, 1.0, 1.5 and 2.0. The range of Reynolds number covered 10000< Re < 50000. The results showed a decrease in drag force coefficients with decreasing aspect ratio, as well as a decrease in Strouhal number. The cylinder was made up of Poly Vinyl Chloride or PVC and with an external diameter of 125mm. It was found that L/D=2.0 had flow dominated by von Kármán street characteristics, not so for lower values. This is because the influence of the structures formed due to the presence of the free end cylinder grows. Therefore, the von Kármán street characteristics diminish with decreasing aspect ratio. Also, the forces in the stream wise direction, x, decrease with decreasing aspect ratio. In the lowest aspect ratio cases, the behaviour is different because of the high influence of the forces due to the free-surface effects.

We can conclude from the literature survey that the study of flow past a cylinder has interested plenty of researchers and attempts have been made in this regard. Further, it should also be noted that researchers are attempting to come up with different

numerical schemes to obtain the solution of the Navier Stokes equation. It can be seen that SIMPLE algorithm is among the common approaches that is employed to obtain the solution of Navier Stokes equation and thus the development of new numerical schemes is based on it. There have been developments in the flow visualising techniques used for the purpose of experimental study wherein there is increased interest to study polymer flows.

Motivation -

Although innumerable experiments conducted throughout the world, experimental fluid mechanics still continues to interest researchers because of its unpredictable nature. Thus to delve into such a challenging field it is imperative to ensure that the basics are understood. In order to improve our basic understanding we are attempting to setup an experiment to study the wakes and vortices of flow past a circular cylinder which is a well understood problem. Also, a solver is being developed which we believe will give is an insight into the field of Computational Fluid Dynamics, thus enabling us to gain an understanding of applied numerical methods. The project thus can be taken as an academic exercise.

Objectives of the current project –

1. To design and fabricate a water channel to perform the study of wakes and vortices of flow past a cylinder.

2. To visualize wakes and vortices at different Reynolds number by means of injecting dyes and capturing the images.

Chapter 3

Design of water channel for experimental study of flow past circular cylinder.

3.1 Description

To study the flow past a circular cylinder experimentally, a fully developed laminar channel flow is required. To obtain such a flow, a water channel has been developed such that laminar flow is obtained at the test section.

The experimental study can also be conducted using a test section with the air as the circulating fluid but the reasons for choosing water over air are –

1. Flow visualisation is easier to conduct when water is the fluid.
2. Measurement of forces is easier as magnitude of the forces acting are higher when water is used as the fluid.

The test cylinder dimensions were decided first, and the channel was designed around that diameter D. Here, $D = 1$" or 25.4 mm was chosen. To ensure only two-dimensional wake flow and avoid three-dimensional effects, a cylinder with aspect ratio or, l/d ratio must be 7 or greater (Norberg, 1994). A length of 12 D was decided. Based on these dimensions, the dimensions of the rest of the test section was decided to minimize any wall and surface effects influencing the flow at the centre of the test section. The standard correlations were obtained from Ferziger and Peric, 2012.

Note that all distances with reference to the cylinder is to the axis of the cylinder. The geometry of the test section is shown in Figure 3.1. Figure 3.2 and 3.3 show the orthographic and isometric view of the experimental setup respectively. Figure 3.4 and 3.5 show the isometric view of the test section and mounting table respectively

18

The channel is essentially a cuboid with an open top. It is decided to be made entirely of Perspex glass to make observations and flow visualisation simple and clear. To minimize wall effects, the distance to the cylinder from the cylinder must be at least $2D$. Hence a total width of $5D$ was chosen. Since the height of the test specimen was decided to be $12D$, to prevent any spillage of water, the channel height was chosen as $13D$. The length of the channel is the sum of all required length of the sections as stated below. All sections were decided to be held together using angle brackets and fasteners with rubber gaskets or sealant glue to prevent leaks. The channel is mounted on a steel table.

As seen in Figure 3.4, the inlet is present at the centre of one of the smaller faces. The flow is allowed to develop in the inlet section of length $6D$. In front of this section is a pack of straws whose function is to ensure laminar, one dimensional flow into the test section that lies beyond the straw section. The length of the straw section is chosen as $10D$.

The length needed for flow visualisation is 20 times the diameter of the cylinder. Hence the distance beyond the cylinder is $20D$. The distance between the straws and the cylinder is $5D$, bringing the total length of the test section to $25D$. Underneath the test section, a 1000W halogen lamp with white background is used for uniform illumination. A DSLR camera is employed to obtain clear shadow images of the flow, the wakes and vortices present downstream.

The far end of the channel will have a pipe connected at the bottom to remove water from the channel. The water is driven by a $^1/_4{}^{\text{th}}$ HP pump that will be below the channel, underneath the table as shown in Figure 3.3. The pump is connected to the two

ends of the channel with a bypass line from the high pressure end to the low pressure end. Gate valves are present in both the main line as well as the bypass line. This bypass line will allow the flow to be controlled to obtain a range of flow rates, hence a range of *Re* values from 0 to 340.
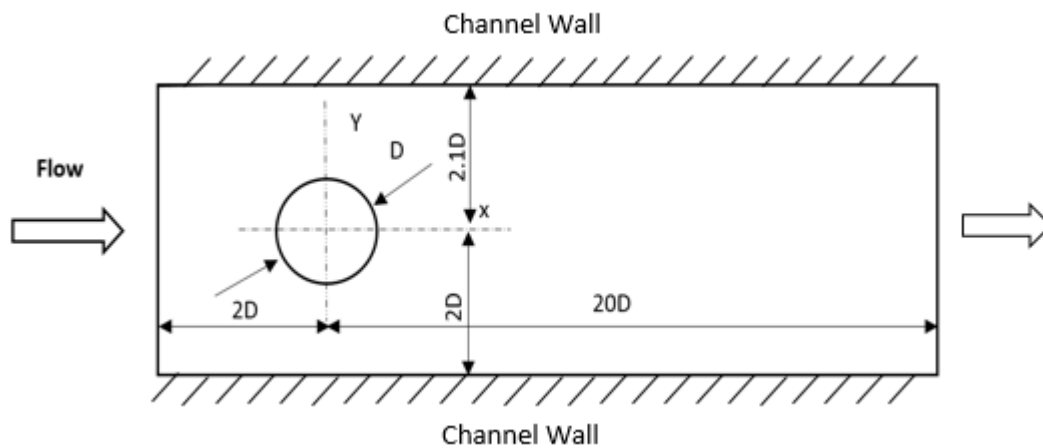

Figure 3.1 - Geometry for laminar flow around a circular cylinder in a channel.

3.2 Calculation of Reynolds Number

For a 0.25 HP pump, Flow rate (Q) = 25 LPM.

Taking diameter of cylinder (D) = 1 inch.

Height of the channel (H) = 12D = 12 inch.

Width of the channel (W) = 5D = 5 inch.

Area of Cross section normal to the flow (A) = H*W =12x 5

$$=60 \text{ sq. inch} = 0.038 \text{ m}^2$$

$$Q = A \times V \tag{1}$$

$V = 0.011 \text{ ms}^{-1}$

20

$$\nu = 0.801 \text{ x } 10^{-6} \, \text{m}^2\text{s}^{-1}$$

$$Re = \frac{V \times d}{\nu} \tag{2}$$

Re = 341.3
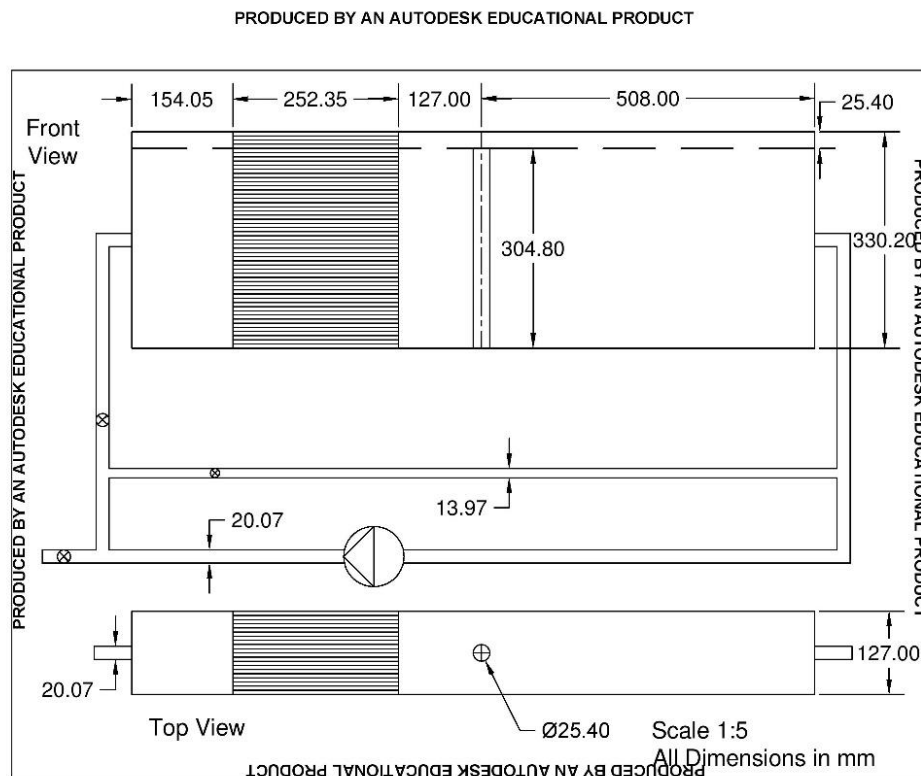
Figure 3.2 - Orthographic projection of the experimental setup.
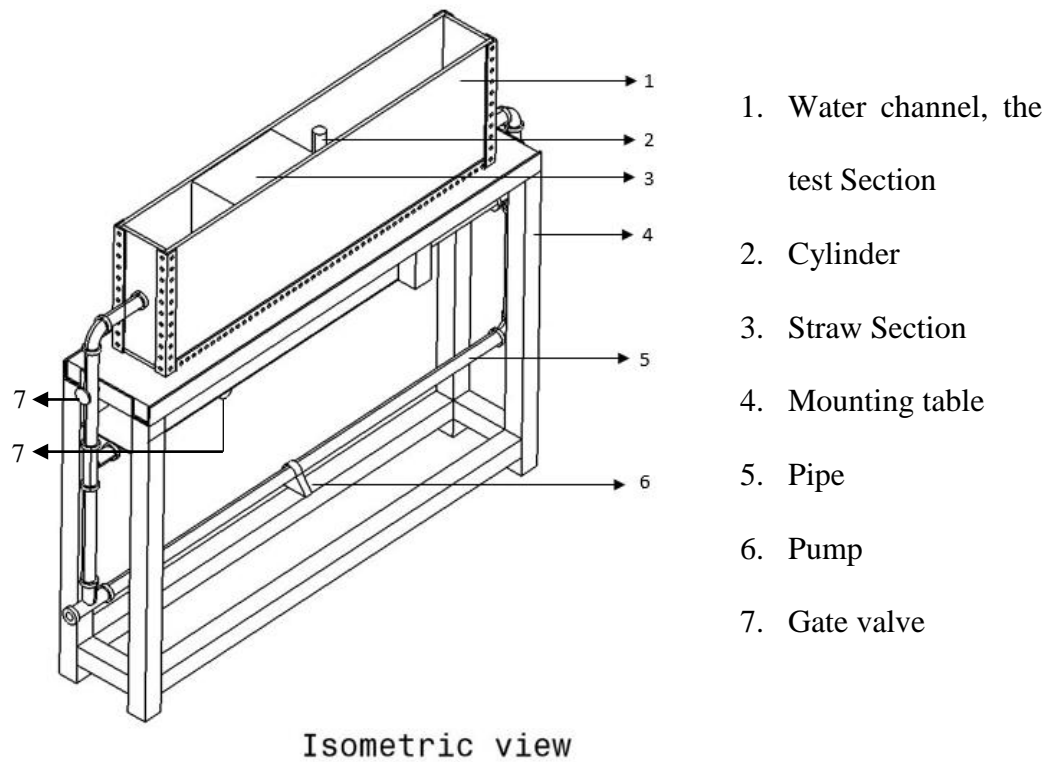
Isometric view

Figure 3.3 - Isometric view of the experimental setup.

1. Water channel, the test Section
2. Cylinder
3. Straw Section
4. Mounting table
5. Pipe
6. Pump
7. Gate valve

127.4

1041.4

330.2

⌀20.07

1. Mild steel angle
2. Perspex sheet

All dimensions in mm
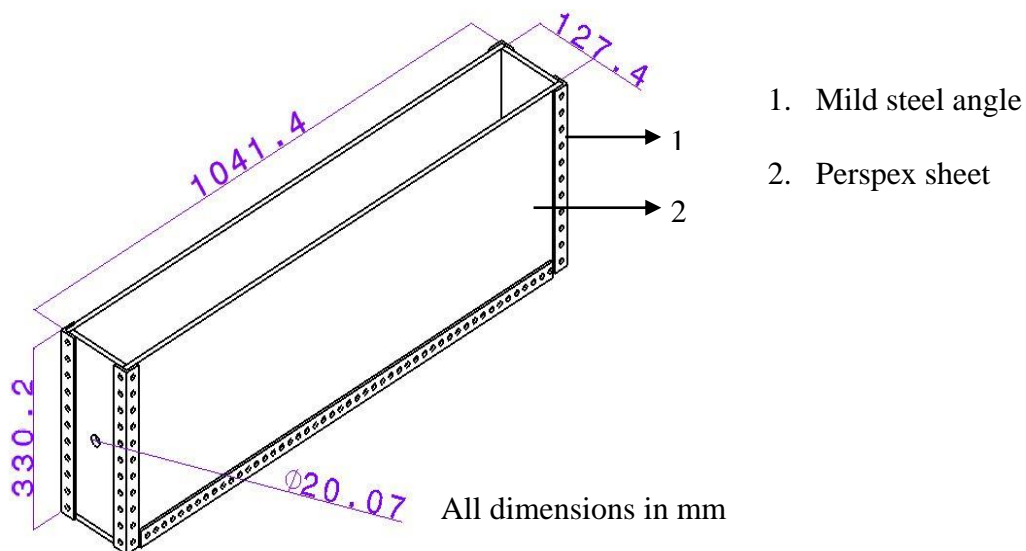
Figure 3.4 - Isometric view of water channel, the test section.

1. Table support legs
2. Opening to provide light

All dimensions in mm

Figure 3.5 - Isometric view of mounting table.

Chapter 4

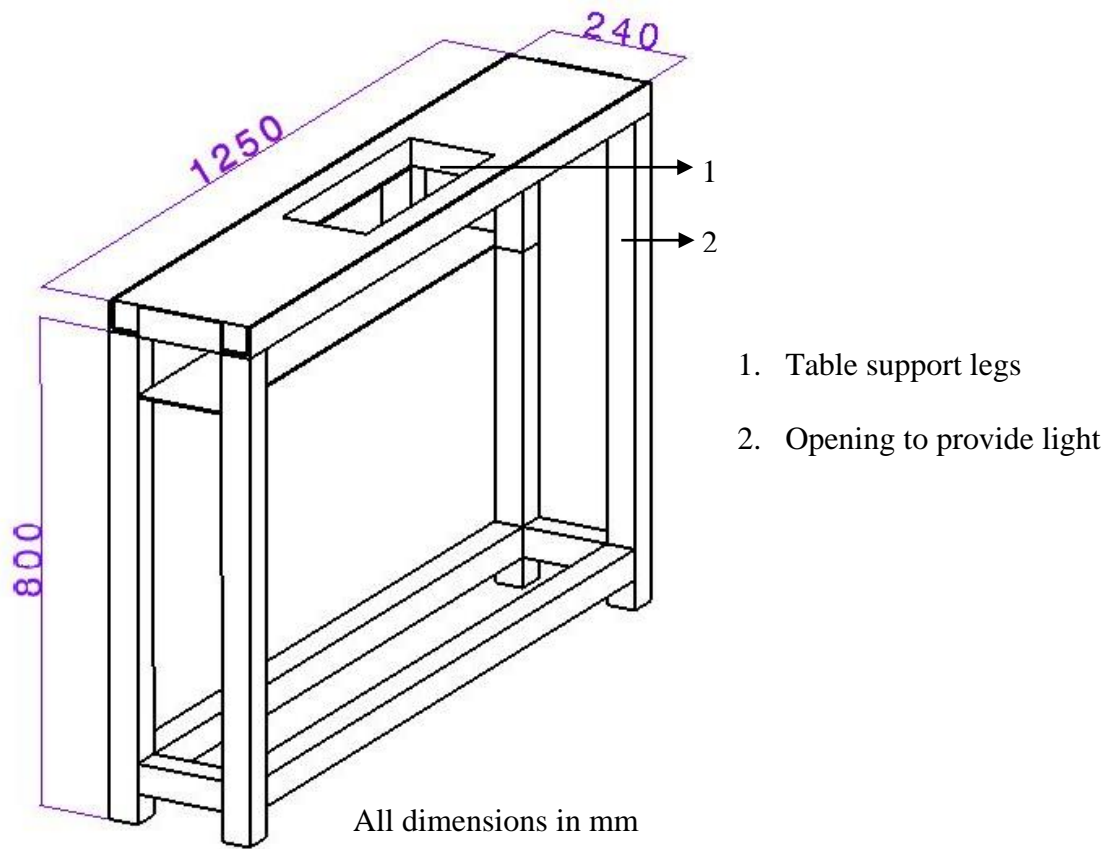## Fabrication and assembly of the experimental setup.

4.1 Fabrication of the test section.

As mentioned in the previous chapter, Perspex glass sheet of thickness $10\ mm$ was chosen as the material used to make the test section. Based on the design of the test section mild steel angles of dimensions 50 mm $\times$ 50 mm and of required length were procured. Rubber gasket was purchased and was cut to the required lengths corresponding to the dimensions of the angles.

Steps followed in the fabrication of the test section were-

1. The Perspex sheet edges were first planed to ensure flatness and maintain parallelism.
2. The location of the fasteners was decided and marked on the Perspex sheet, rubber gasket and the angles.
3. Holes of size M8 were drilled at the marked locations on the angles using the bench drilling machine and a hand drill was used to drill the holes on the gasket and the Perspex sheet.
4. The test section was then assembled using high grade fasteners.

The assembled test section is as shown in the Figure 4.1. As shown, it consists of the Perspex sheets held together supported by the mild steel angles.

4.2 Setting up the straw section

The experimental setup requires the use of a straw section to modify the flow from turbulent at the inlet to laminar upstream of the bluff body. The straw section

consists of thin aluminium sheets. Two sheets of dimensions $250\ mm \times 300\ mm$ and one sheet of size $250\ mm \times 125\ mm$ were used and they were held together by means of L clamps. The straws were then placed uniformly and a layer of Araldite silicone sealant was applied in between two straws. The process was repeated until the straws were raised to the required height. The Figure 4.2 shows the completed straw section.
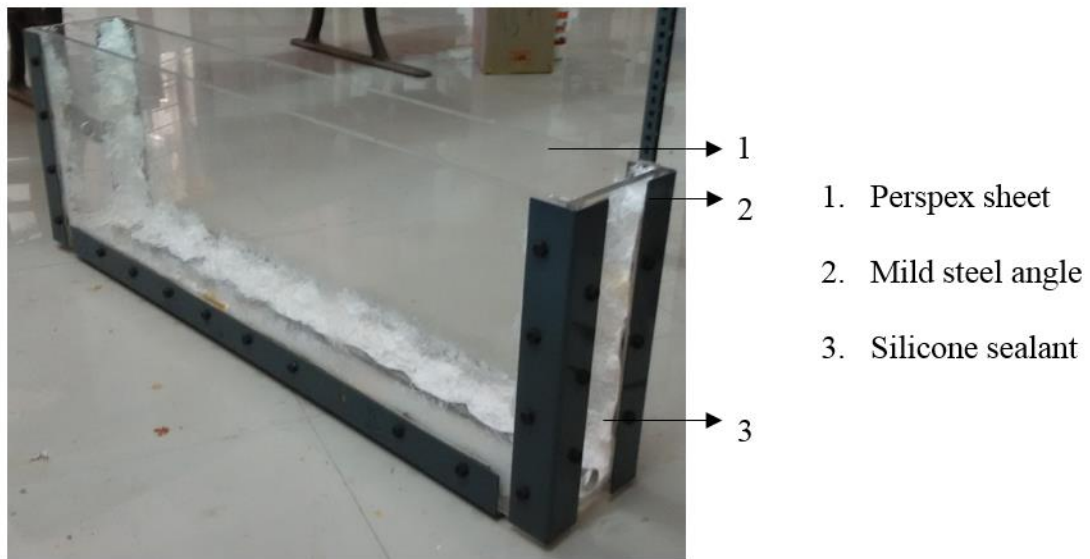

1. Perspex sheet
2. Mild steel angle
3. Silicone sealant

Figure 4.1- Isometric view of the assembled test section.
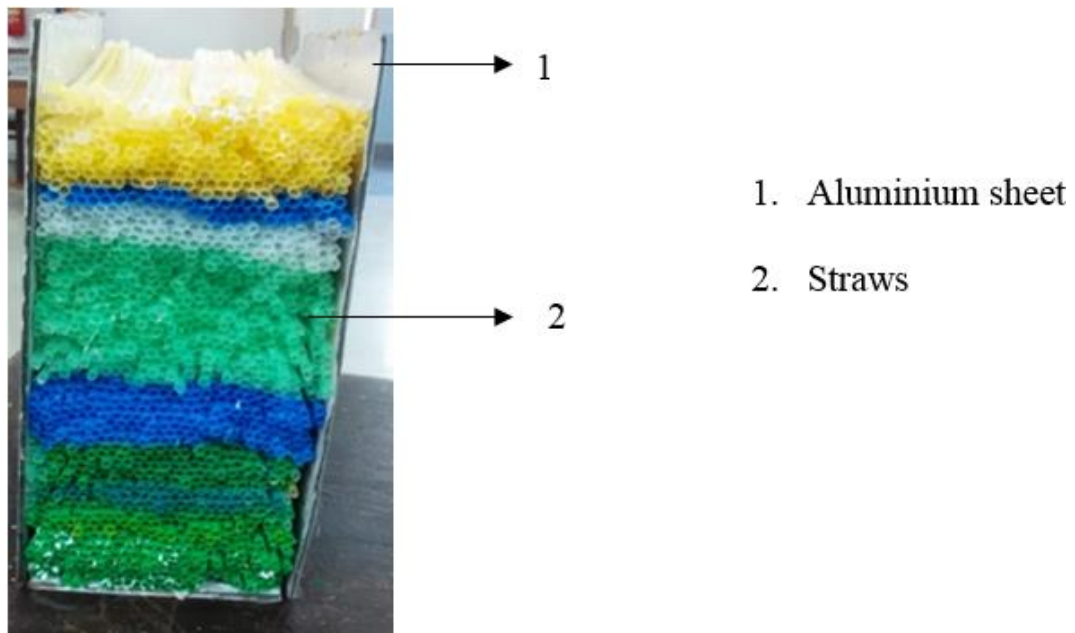

1. Aluminium sheet
2. Straws

Figure 4.2 - Side view of the straw section.

4.3 Assembly of experimental setup

The remaining components of the setup such as the piping system, required pipe fittings such as elbows, T-joint, tank nipple and gate valves were first assembled along with the table. The pipes and the pipe fittings were made of CPVC. A length of 3050 mm of diameter $3/4$ $inch$ was used for the main line. A length of 1050 mm of diameter $1/4$ $inch$ was used for the bypass line. The main line, bypass line are connected to the pump and the water channel using three elbows, three T-joints and two tank nipples. The pipe fittings were connected to the pipes using CPVC pipe adhesive. The state of the assembled system at his stage is shown in the Figure 4.3. It can be seen that the bypass line is connected to the main line using the T-joint and the gate valves are provided to control flow rates. Further, the test section and the straw section were also assembled and silicone sealant was applied to prevent leaks. The final assembled system was obtained as shown in the Figure 4.4.

1. Gate Valve
2. T-joint
3. Main line
4. Elbow
5. Opening for visualization
6. Table
7. Bypass line
8. Ball valve
9. Pump
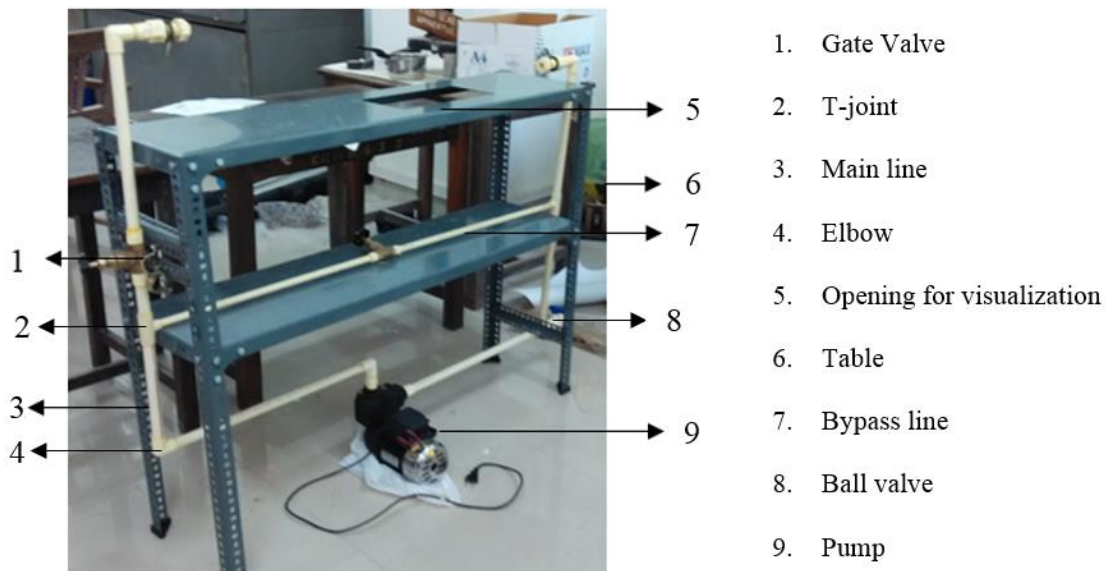
Figure 4.3 - View of the assembled table and piping.

1. Test section
2. Straw section
3. Table
4. Bypass line
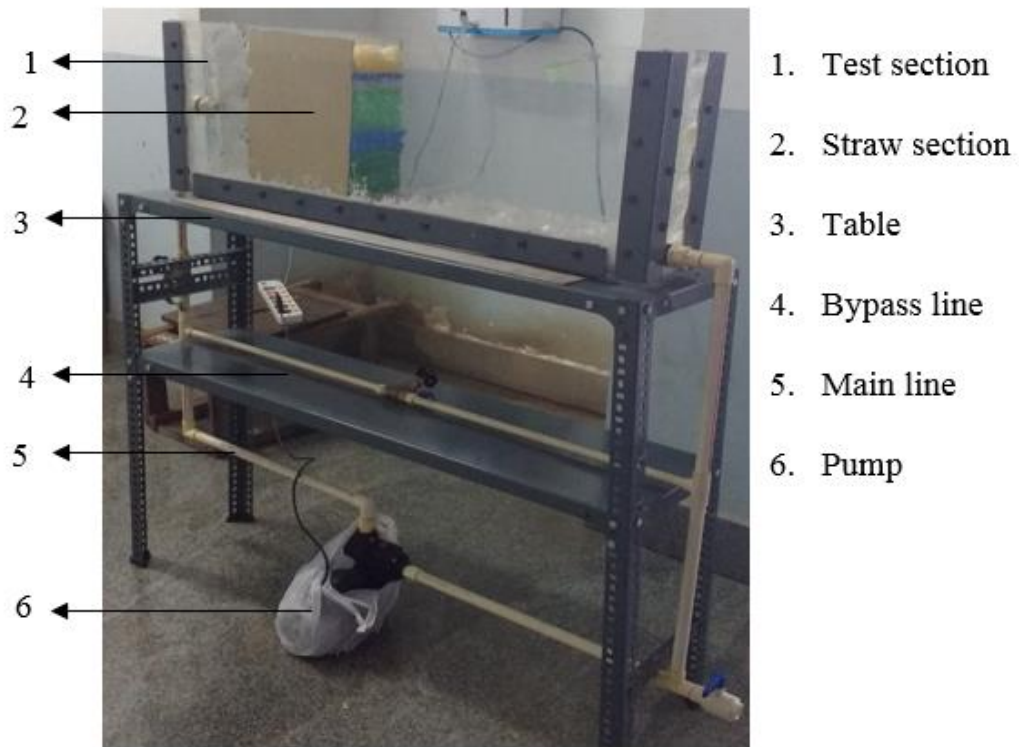5. Main line
6. Pump

Figure 4.4 - Image of the completely assembled experimental setup.

Chapter 5

Experimental procedure to visualize the flow past a circular cylinder

Following the fabrication and assembly of the experimental setup that was described in the previous chapter, the low speed water channel was used to conduct the flow visualisation experiments to observe the flow pattern around a cylinder.

Consider the Figure 5.1, to conduct the experiments water is filled into the system up to the required height in the test section by means of a ball valve that is provided at the bottom of the setup. This valve also serves the purpose of draining the water out of the system after the completion of the experiments. The centrifugal pump is used to drive the water flow in the system. The flow rate of water inside the test section can be varied using the two gate valves that are provided in the main line and the bypass line respectively. The relative positions of these two gate valves dictate the rate at which the flow enters the test section.

1. Test section
2. Straw section
3. Table
4. Bypass line
5. Main line
6. Pump

Figure 5.1 - Experimental Setup.

The flow from the delivery side of the pump passes through the pipe which then expands into the rectangular test section. The flow then is made to pass through the straw section to ensure that the vortical structures and eddies created by the centrifugal pump are minimised and a fully developed laminar flow is obtained downstream of the straw section. The test specimen is placed downstream of the straw section at a distance of 127 mm from the straw section. The test specimen, in our case a circular cylinder is placed at this location. As shown in Figure 5.2 the circular cylinder is mounted on an acrylic sheet to prevent it from toppling due to the water flow and it is placed at the required location.
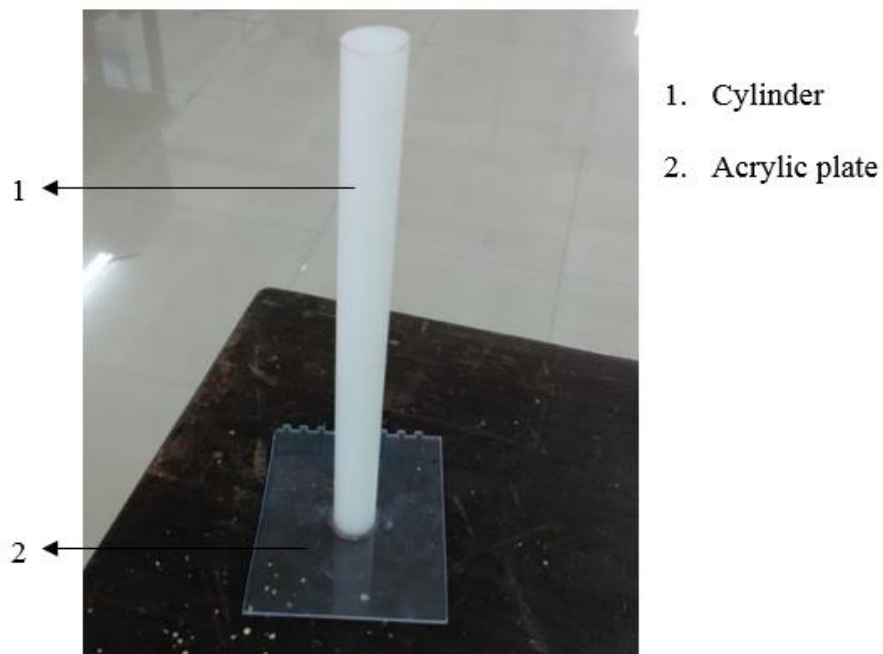

Figure 5.2- Nylon circular cylinder with a
flat acrylic base.

The transparent acrylic walls of the test section allow for flow visualisation through both top and front views. The test section is cleaned using isopropanol and kerosene before the experiment to minimise surface roughness.

The flow velocity for each test case at which the experiment was performed was calculated by measuring the flow rate at the inlet of the test section. A pipe of diameter $2\ mm$ was inserted into the flow at the centreline and a volume of $50\ mm$ was collected and the time taken was measured. This gave the volumetric flow rate. Using equation 3, flow velocity was calculated and subsequently the Reynolds number was calculated using the equation 4.

$$V = \frac{Q}{A} \tag{3}$$

$$Re = \frac{V \times d}{\nu} \tag{4}$$

Flow visualisation was performed using coloured fountain pen ink as dye. Red and blue coloured ink were used as dyes. The inks were injected using two hypodermic needles mounted at the stagnation point of the cylinder. Ink was supplied to the needles by means of IV lines which in turn were connected to two bottles which acted as reservoirs for red and blue inks. Flow of inks was controlled using valves provided in the IV line. The needle had a diameter of $0.26\ mm$.

Imaging was done using a Canon EOS 550D DSLR camera. Canon 18-55 mm stock lens was used with a focal length of $30\ mm$ for top view imaging. The following camera settings were used: ISO 800, aperture F5.6 and a shutter speed of $^1/_{250}$. The field of view was about $200\ mm \times 100\ mm$. As shown in Figure 5.3, a

30

1000 W halogen lamp was used to provide uniform background lighting. A white coloured background paper was kept under the test section to diffuse the light source.
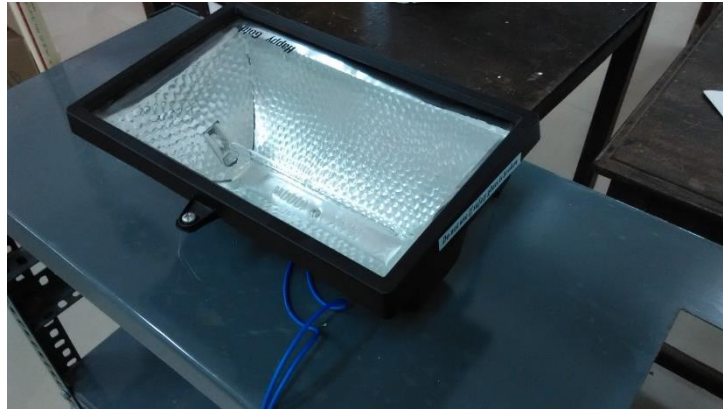

Figure 5.3 - 1000 W halogen lamp.

Chapter 6

Flow visualization of flow past a circular cylinder

The flow visualisation experiments were performed based on the experimental procedure described in the previous chapter. The images from the flow visualization at different Reynolds number are described further. Experiments were conducted for Reynolds number of $46, 155$ *and* 255. Six trials were conducted for each Reynolds number and the best images that were captured are presented in chapter. These images were further used to calculate flow separation angle.

Angle of separation is the angle the line joining the point of separation and the axis of the cylinder makes with the line joining the stagnation point and the axis.
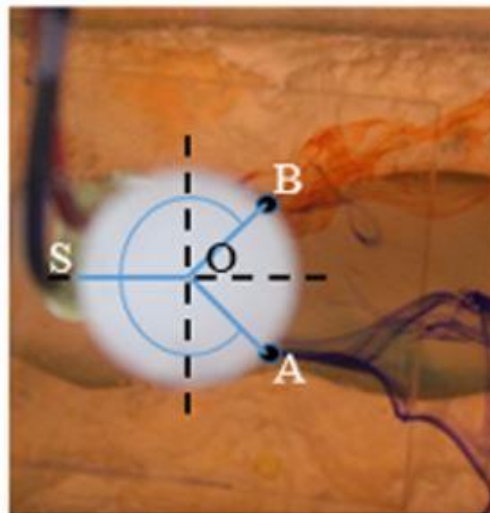
O - Axis centre.

S - Stagnation point.

A, B - Poin s of separation.

$\angle SOB$ - Angle of separation of point red ink at B.

$\angle SOA$ - Angle of separation of point blue ink at A.
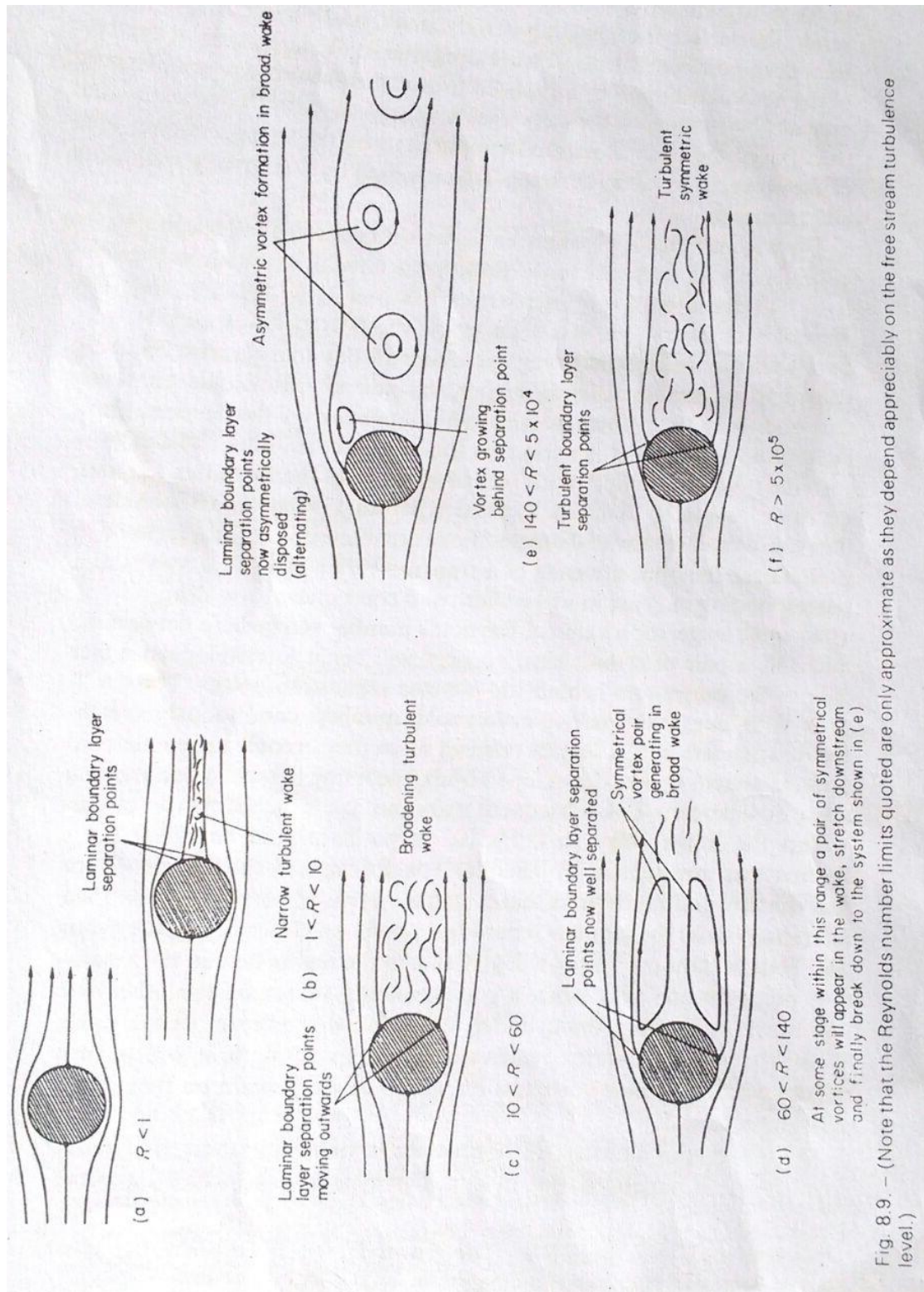
Figure 6.1 - Calculation of angle of separation.

Figure 6.2 - Flow regimes past a circular cylinder. (Image taken from Aerodynamics for engineering students, by Houghton and Carpenter. Fourth edition, published by Butterworth Heinemann).

33

Figure 6.2 shows patterns of wakes and vortices for a flow past a circular cylinder at various Reynolds number ranges which were used to compare with the flow visualization images obtained by the experiments. The experimental results seem to be in good agreement with the patterns shown in the figure 6.2.

6.1 Reynolds number 46

The figures 6.3, 6.4 and 6.5 show the flow visualisation patterns that were obtained for $Re=46$. In figure 6.3 the blue dye clearly shows the delayed separation of
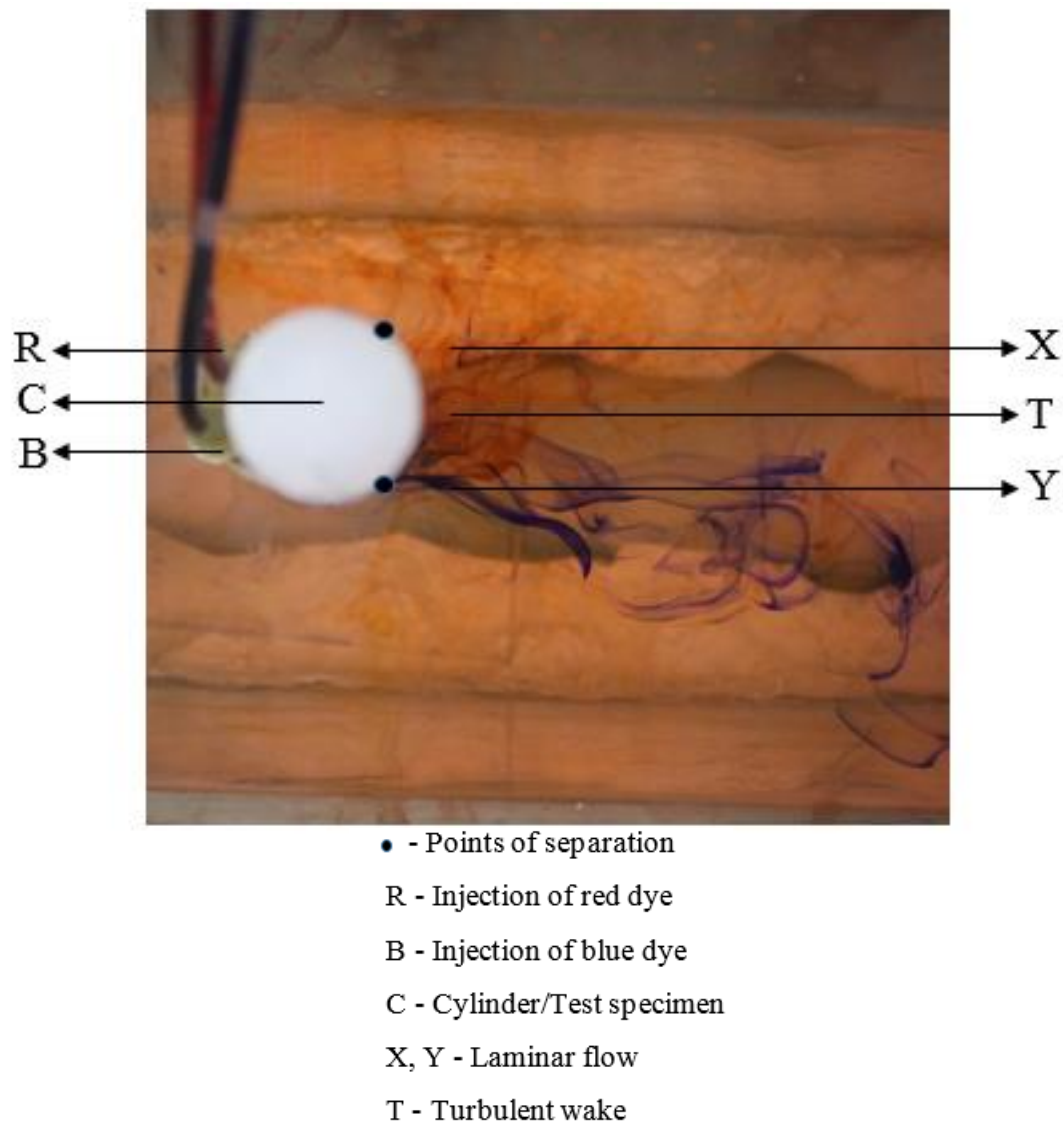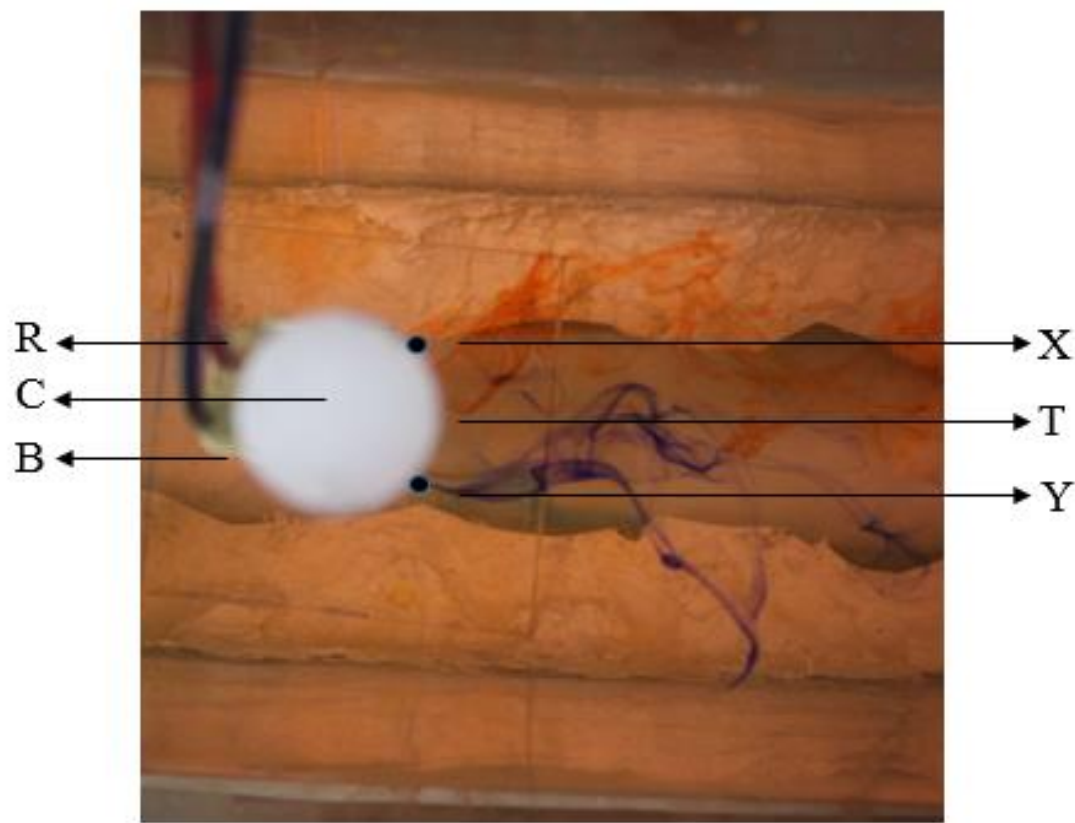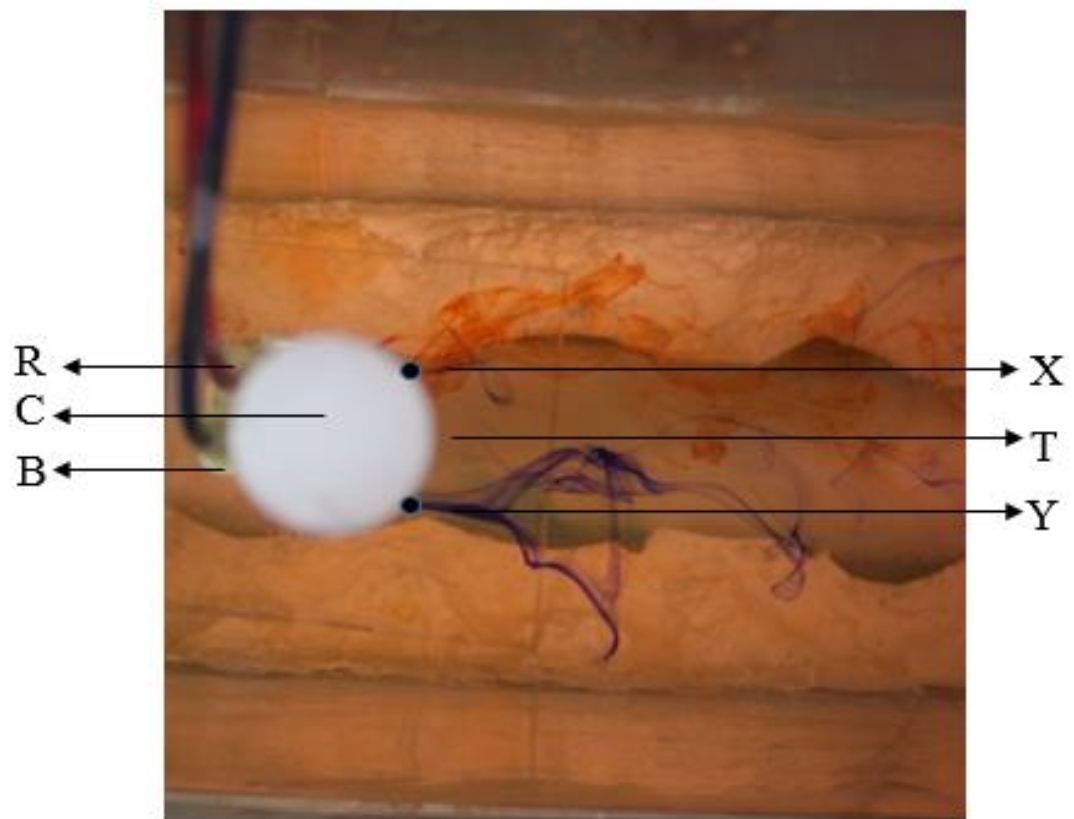

• - Points of separation
R - Injection of red dye
B - Injection of blue dye
C - Cylinder/Test specimen
X, Y - Laminar flow
T - Turbulent wake

Figure 6.3 - Flow visualization image 1 at Re =46.

the boundary layer whereas the red ink gets diffused in a clear pattern cannot be visualized. However in the figure 6.4 the boundary layer separation can be visualized to an extent using red dye. The turbulence region in the wake can also be observed. In figure 6.5 it can be observed that the blue dye follows the laminar flow pattern whereas the red dye is getting diffused. On comparison with the available literature it can be determined that the results obtained at $Re = 46$ belong to the flow regime which is laminar and has a narrow turbulent wake. The significant observations made were that the boundary separation points were symmetric across the streamwise diameter and there was a formation of narrow turbulent wake. The boundary layer separation was found to occur at angles 137°, 138° and 139° with respect to the stagnation point respectively for images shown by Figure 6.3, 6.4 and 6.5.

• - Points of separation

R - Injection of red dye

B - Injection of blue dye

C - Cylinder/Test specimen

X, Y - Laminar flow

T - Turbulent wake

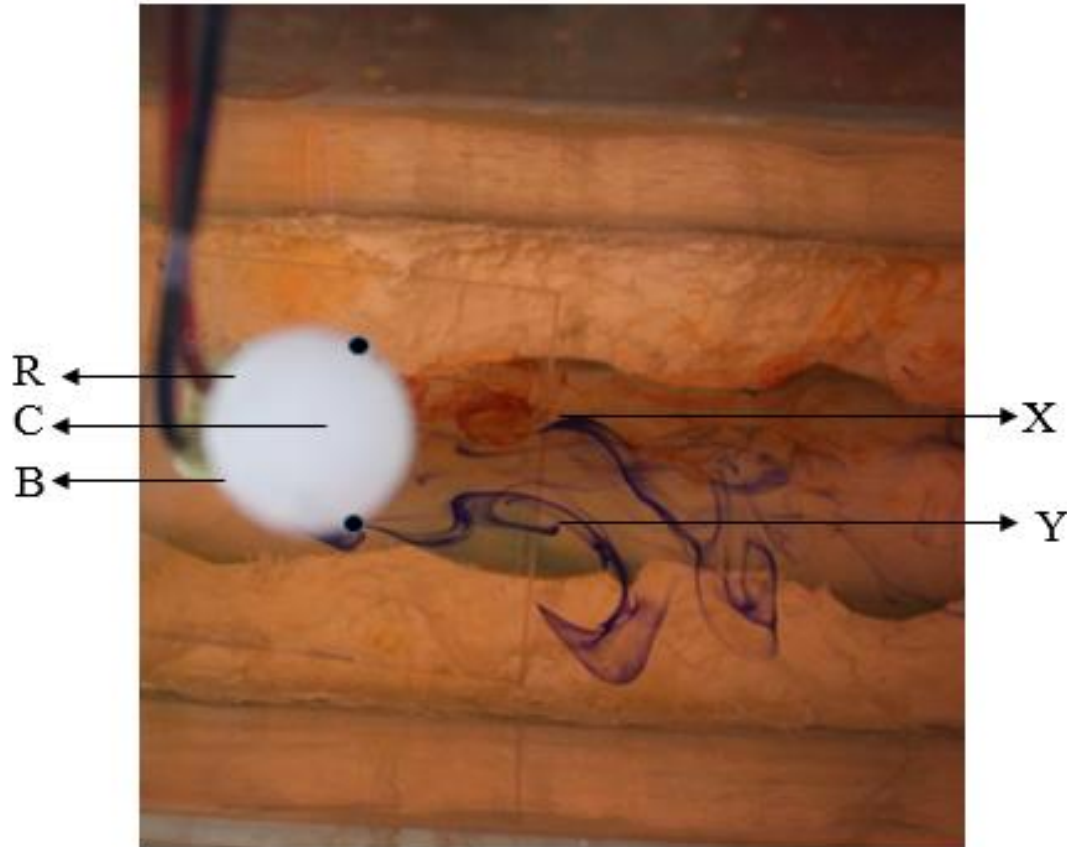Figure 6.4- Flow visualization image 2 at Re =46.

• - Points of separation

R - Injection of red dye

B - Injection of blue dye

C - Cylinder/Test specimen

X, Y - Laminar flow

T - Turbulent wake

Figure 6.5 - Flow visualization image 3 at $Re = 46$.

6.2 Reynolds number 155

• - Points of separation
R - Injection of red dye
B - Injection of blue dye
C - Cylinder/Test specimen
X, Y - Standing vortices

Figure 6.6 - Flow visualization image 1 at *Re* =155.

The figures 6.6, 6.7 and 6.8 show the flow visualization pattern obtained for *Re*=155. On comparison with the available literature it is determined that the flow pattern obtained at this Reynolds number range has a characteristic of having symmetric vortices present in the wake. Figure 6.7 shows a pair of symmetric standing vortices

• - Points of separation

R - Injection of red dye

B - Injection of blue dye

C - Cylinder/Test specimen

X, Y - Standing vortices

Figure 6.7 - Flow visualization image 2 at *Re* =155.

behind the cylinder. In figure 6.8, the vortex visualized by the blue dye has developed more compared to the vortex shown by the red dye. In figure 6.9, the flow represented by blue dye has undergone flow separation earlier than the flow represented by red dye. As a result, the blue dye has diffused faster. The figures 6.6, 6.7 and 6.8 have angles of separation were found to be 116°, 110° and 105° respectively with respect to

stagnation point. The images show the formation of a pair of vortices in the wake. It can be seen that thereafter the wake becomes turbulent.
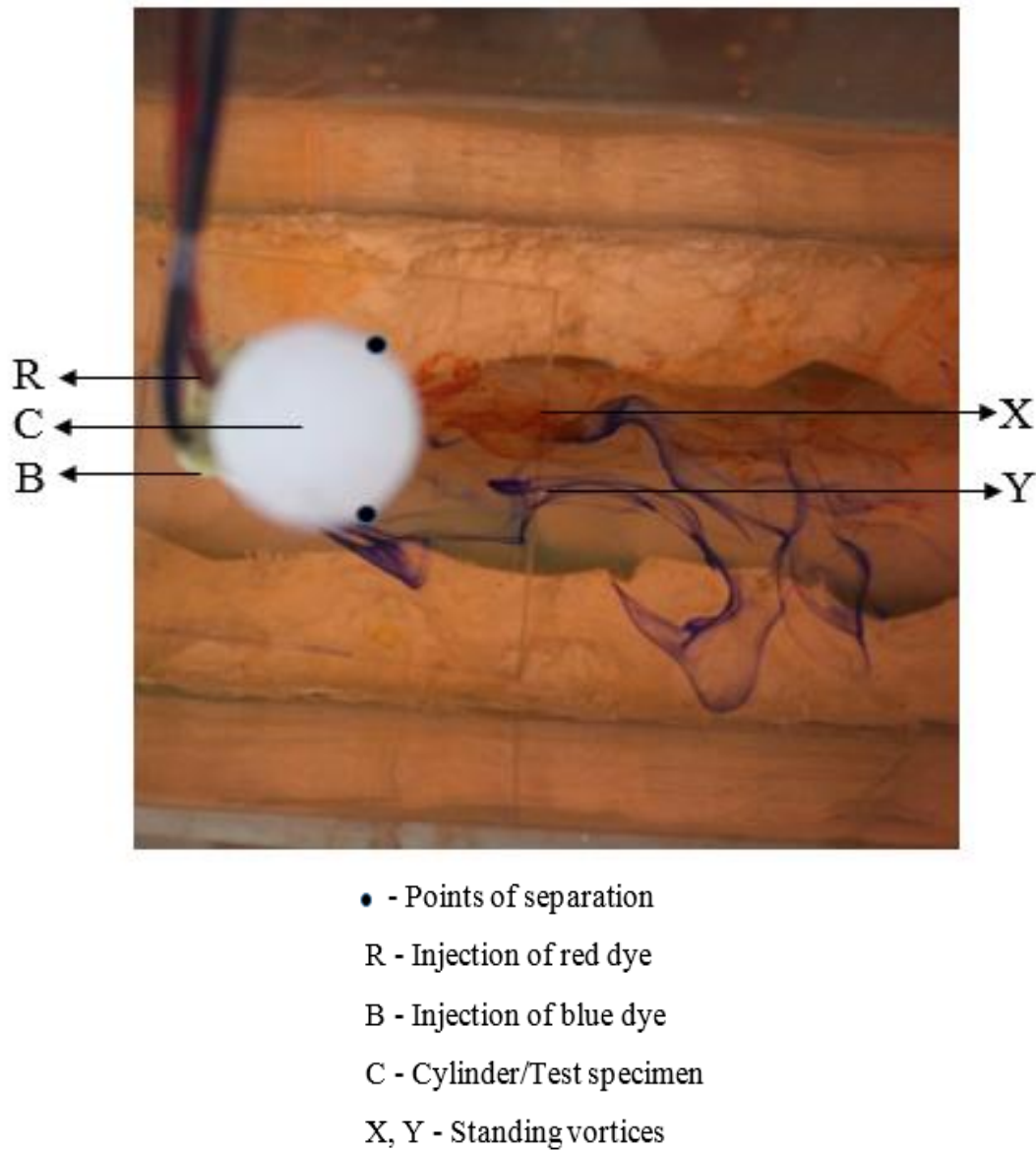

• - Points of separation

R - Injection of red dye

B - Injection of blue dye

C - Cylinder/Test specimen
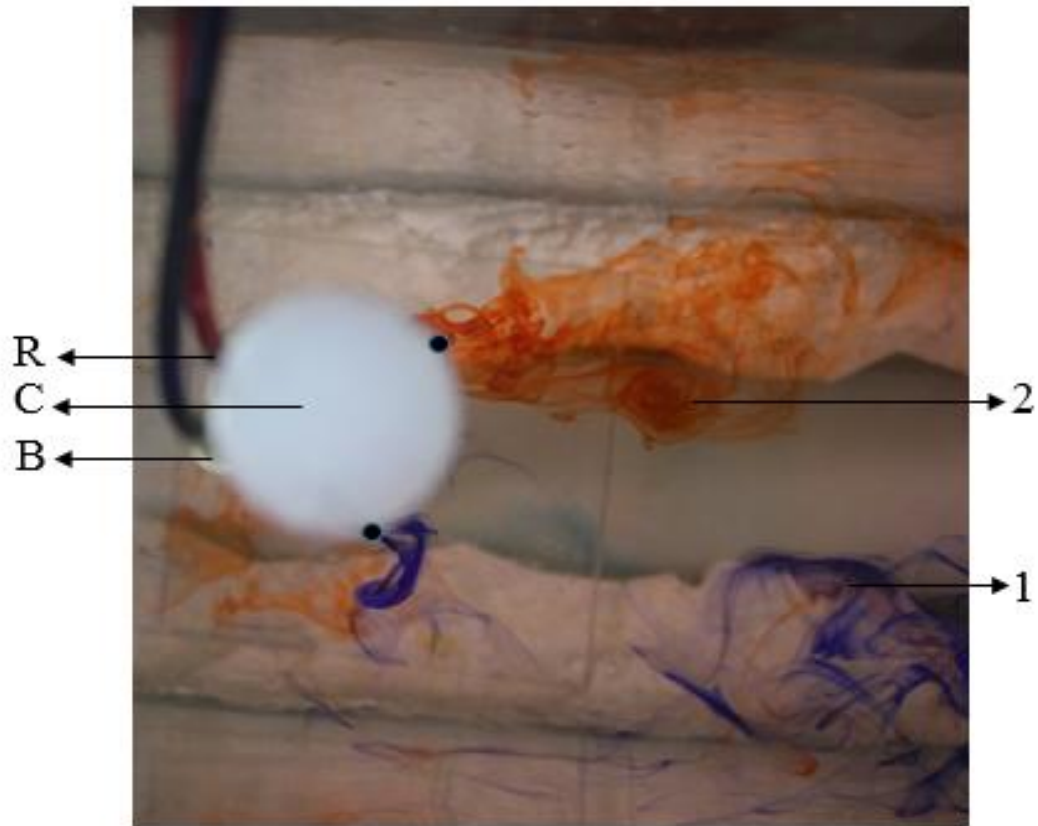
X, Y - Standing vortices

Figure 6.8 - Flow visualization image 3 at *Re* =155.

6.3 Reynolds number 255

The figures 6.9, 6.10 and 6.11 show the flow visualization pattern obtained for *Re*=255. The flow visualisation obtained at this Reynolds number is known as Von
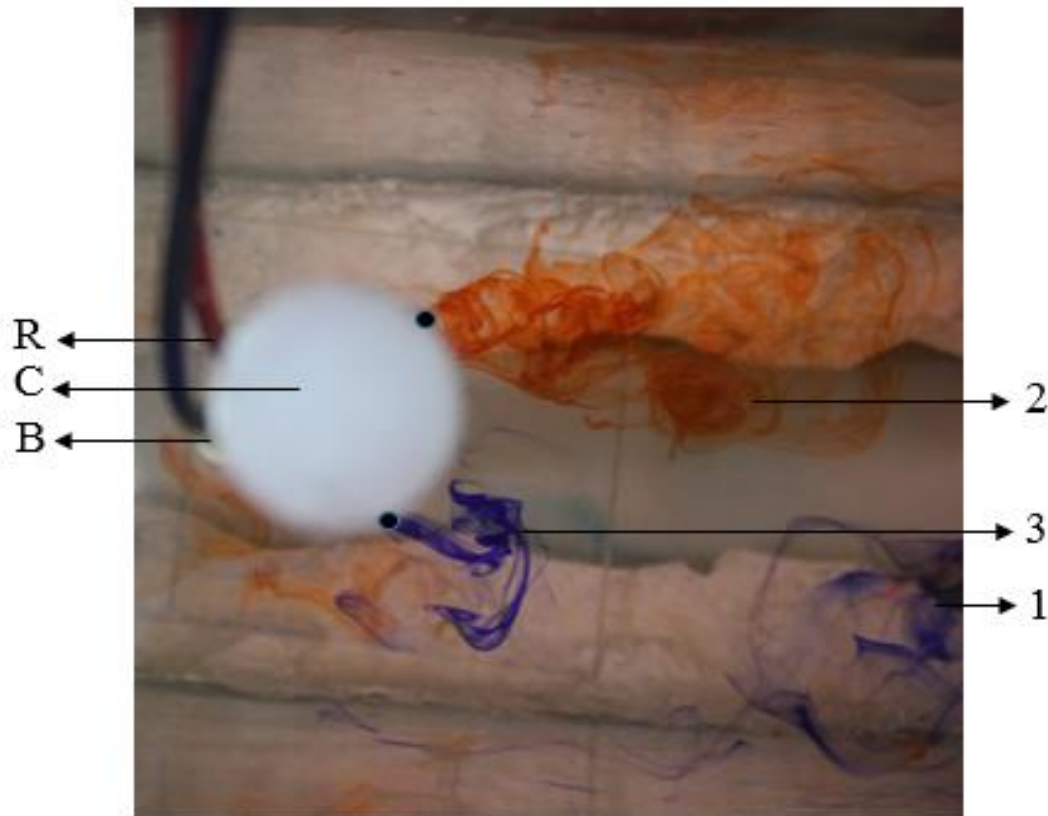
• - Points of separation
R - Injection of red dye
B - Injection of blue dye
C - Cylinder/Test specimen
1 - Vortex 1
2 - Vortex 2

Figure 6.9 - Flow visualization image 1 at *Re* =255.

Karman vortex street. The important observations made were: the boundary layer separation is asymmetric across the cylinder centreline in the stream wise direction. As evident from the figures, there is an alternate shedding of vortices from the cylinder. The figures 6.9, 6.10 and 6.11 were images captured in order. Fig 6.9 shows the vortex above the centreline which is visualized using red dye, whereas below the centreline

the blue dye shows the flow separation occurring. Fig 6.10, the image shows both alternating vortices clearly. In Fig 6.11 the flow separation is taking place which is shown by the red dye.

- • - Points of separation
- R - Injection of red dye
- B - Injection of blue dye
- C - Cylinder/Test specimen
- 1 - Vortex 1
- 2 - Vortex 2
- 3 - Vortex 3

Figure 6.10 - Flow visualization image 2 at *Re* =255.

• - Points of separation

R - Injection of red dye

B - Injection of blue dye

C - Cylinder/Test specimen

2 - Vortex 2

3 - Vortex 3
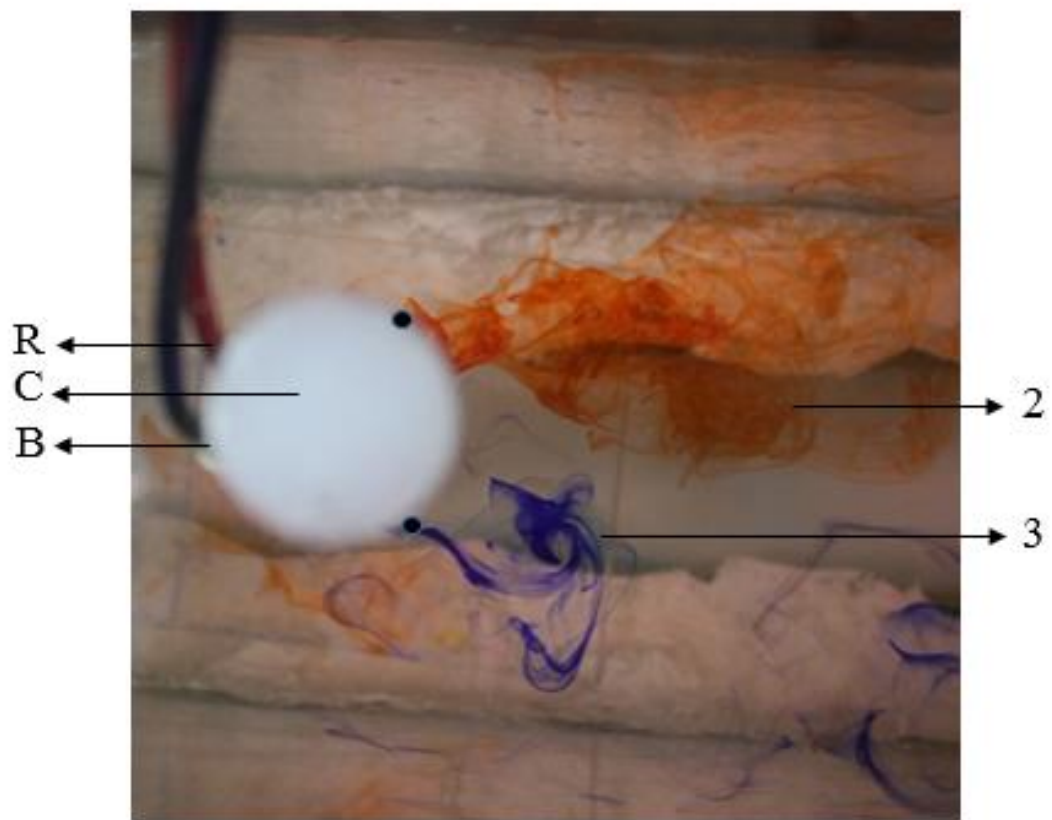
Figure 6.11 - Flow visualization image 3 at Re =255

Chapter 7

Navier-Stokes solver using finite difference method

7.1 Finite Difference Method

Finite-difference methods (FDM) are numerical methods for solving differential equations by approximating them with difference equations, in which finite differences approximate the derivatives. The governing equations are discretised using this method.

An explicit scheme is used where the forward difference scheme is used for the time derivative and backward difference scheme is used for the space derivative. The second-order derivative is discretised using a central difference scheme. For incompressible flows, there is no obvious way to couple velocity and pressure. Divergence of momentum equation is taken and continuity equation is used to get a Poisson's equation for pressure.

A method of solving Poisson's equation for pressure was developed by Harlow and Welch (1965) and has been frequently used to obtain pressure field, mostly for explicit methods. The proposed computational procedure was to choose the pressure field such that continuity is satisfied at the next time level, so that the new velocity field will be divergence free. One of the shortcomings of this process is that it requires a relaxation scheme while iterating the pressure field until a divergence free velocity field is obtained. Derivation of the pressure-poisson equation is given in Appendix A.

Advantage of explicit approach is that it is relatively simple to set up and program. However, for a given Δx, Δt must be less than some limit imposed by stability constraints. In some cases, Δt must be very small to maintain stability; this can result in longer computer running times to make calculations over a given interval of t.

7.2 Governing Equations

1. U momentum equation

$$\frac{\partial u}{\partial t} + u\frac{\partial u}{\partial x} + v\frac{\partial u}{\partial y} = -\frac{1}{\rho}\frac{\partial p}{\partial x} + v\left(\frac{\partial^2 u}{\partial x^2} + \frac{\partial^2 u}{\partial y^2}\right) \qquad (4)$$

2. V momentum equation

$$\frac{\partial v}{\partial t} + u\frac{\partial v}{\partial x} + v\frac{\partial v}{\partial y} = -\frac{1}{\rho}\frac{\partial p}{\partial y} + v\left(\frac{\partial^2 v}{\partial x^2} + \frac{\partial^2 v}{\partial y^2}\right) \qquad (5)$$

3. Pressure Poisson's equation

$$\frac{\partial^2 u}{\partial x^2} + \frac{\partial^2 v}{\partial y^2} = -\rho\left(\frac{\partial u}{\partial x}\frac{\partial u}{\partial x} + 2\frac{\partial u}{\partial y}\frac{\partial v}{\partial x} + \frac{\partial v}{\partial y}\frac{\partial v}{\partial y}\right) \qquad (6)$$

7.3 Discretized Equations

1. Discretized U momentum equation

$$\frac{u_{i,j}^{n+1} - u_{i,j}^{n}}{\Delta t} + u_{i,j}^{n}\frac{u_{i,j}^{n} - u_{i-1,j}^{n}}{\Delta x} + v_{i,j}^{n}\frac{u_{i,j}^{n} - u_{i-1,j}^{n}}{\Delta y}$$

$$= -\frac{1}{\rho}\frac{p_{i+1,j}^{n} - p_{i-1,j}^{n}}{2\Delta x}$$

$$+ v\left(\frac{u_{i+1,j}^{n} - 2u_{i,j}^{n} + u_{i-1,j}^{n}}{\Delta x^2}\right.$$

$$\left. + \frac{u_{i+1,j}^{n} - 2u_{i,j}^{n} + u_{i-1,j}^{n}}{\Delta y^2}\right) \qquad (7)$$

2. Discretized V momentum equation

$$\frac{v_{i,j}^{n+1} - v_{i,j}^n}{\Delta t} + u_{i,j}^n \frac{v_{i,j}^n - v_{i-1,j}^n}{\Delta x} + v_{i,j}^n \frac{v_{i,j}^n - v_{i-1,j}^n}{\Delta y}$$

$$= -\frac{1}{\rho} \frac{p_{i+1,j}^n - p_{i-1,j}^n}{2\Delta y}$$

$$+ \nu \left(\frac{v_{i+1,j}^n - 2v_{i,j}^n + v_{i-1,j}^n}{\Delta x^2} \right.$$

$$\left. + \frac{v_{i+1,j}^n - 2v_{i,j}^n + v_{i-1,j}^n}{\Delta y^2} \right)$$

(8)

3. Discretized Pressure Poisson equation

$$\frac{p_{i+1,j}^n - 2p_{i,j}^n + p_{i-1,j}^n}{\Delta x^2} + \frac{p_{i+1,j}^n - 2p_{i,j}^n + p_{i-1,j}^n}{\Delta y^2}$$

$$= \rho \left[\frac{1}{\Delta t} \left(\frac{u_{i+1,j} - u_{i-1,j}}{2\Delta x} + \frac{v_{i+1,j} - v_{i-1,j}}{2\Delta y} \right) \right.$$

$$- \frac{u_{i+1,j} - u_{i-1,j}}{2\Delta x} \frac{u_{i+1,j} - u_{i-1,j}}{2\Delta x}$$

(9)

$$- 2 \frac{u_{i+1,j} - u_{i-1,j}}{2\Delta y} \frac{v_{i+1,j} - v_{i-1,j}}{2\Delta x}$$

$$\left. - \frac{v_{i+1,j} - v_{i-1,j}}{2\Delta y} \frac{v_{i+1,j} - v_{i-1,j}}{2\Delta y} \right]$$

By rearranging the above equations the momentum equation in the x direction

$$
\begin{aligned}
u_{i,j}^{n+1} = u_{i,j}^n &- u_{i,j}^n \frac{\Delta t}{\Delta x} \left(u_{i,j}^n - u_{i-1,j}^n \right) - v_{i,j}^n \frac{\Delta t}{\Delta x} \left(u_{i,j}^n - u_{i-1,j}^n \right) \\
&- \frac{\Delta t}{\rho 2 \Delta x} \left(p_{i+1,j}^n - p_{i-1,j}^n \right) \\
&+ v \left(\frac{\Delta t}{\Delta x^2} \left(u_{i+1,j}^n - 2u_{i,j}^n + u_{i-1,j}^n \right) \right. \\
&+ \left. \frac{\Delta t}{\Delta y^2} \left(u_{i,j+1}^n - 2u_{i,j}^n + u_{i,j-1}^n \right) \right)
\end{aligned}
\tag{10}
$$

Similarly, the momentum equation in the y direction

$$
\begin{aligned}
v_{i,j}^{n+1} = v_{i,j}^n &- u_{i,j}^n \frac{\Delta t}{\Delta x} \left(v_{i,j}^n - v_{i-1,j}^n \right) - v_{i,j}^n \frac{\Delta t}{\Delta x} \left(v_{i,j}^n - v_{i-1,j}^n \right) \\
&- \frac{\Delta t}{\rho 2 \Delta x} \left(p_{i+1,j}^n - p_{i-1,j}^n \right) \\
&+ v \left(\frac{\Delta t}{\Delta x^2} \left(v_{i+1,j}^n - 2v_{i,j}^n + v_{i-1,j}^n \right) \right. \\
&+ \left. \frac{\Delta t}{\Delta y^2} \left(v_{i,j+1}^n - 2v_{i,j}^n + v_{i,j-1}^n \right) \right)
\end{aligned}
\tag{11}
$$

Now, rearranging the pressure – poisson equation

$$p_{i,j}^n = \frac{\left(p_{i+1,j}^n + p_{i-1,j}^n\right)\Delta y^2 + \left(p_{i,j+1}^n + p_{i,j-1}^n\right)\Delta x^2}{2(\Delta x^2 + \Delta y^2)}$$

$$-\frac{\rho\,\Delta x^2 \Delta y^2}{2(\Delta x^2 + \Delta y^2)}\left[\frac{1}{\Delta t}\left(\frac{u_{i+1,j} - u_{i-1,j}}{2\Delta x}\right.\right.$$

$$+\frac{v_{i+1,j} - v_{i-1,j}}{2\Delta y}\right)$$

$$-\frac{u_{i+1,j} - u_{i-1,j}}{2\Delta x}\frac{u_{i+1,j} - u_{i-1,j}}{2\Delta x}$$

$$-2\frac{u_{i+1,j} - u_{i-1,j}}{2\Delta y}\frac{v_{i+1,j} - v_{i-1,j}}{2\Delta x}$$

$$\left.-\frac{v_{i,j+1} - v_{i,j-1}}{2\Delta y}\frac{v_{i,j+1} - v_{i,j-1}}{2\Delta y}\right]$$

(12)

Solving the above three equations in both time and space after assigning the required initial and boundary conditions gives us both pressure field and velocity field. The solution algorithm is shown in Figure 7.1.
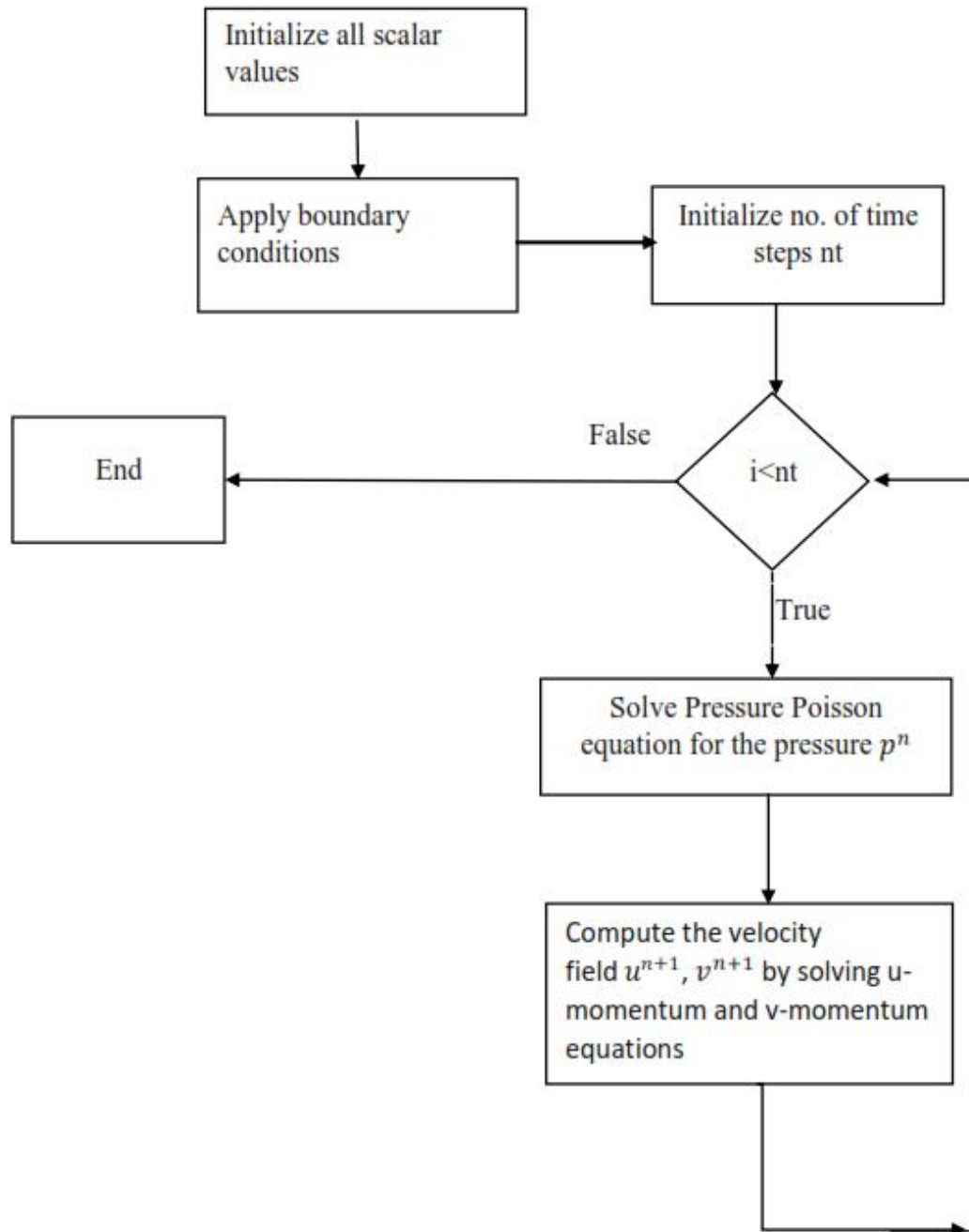
7.4 Solution Algorithm

Figure 7.1 - Solution algorithm for finite difference method formulation.

Chapter 8

Test Cases and their validation

8.1 Lid Driven Cavity

Lid driven cavity serves as a simple and straightforward validation test case for a newly developed CFD solver. The flow is internal and recirculating type. Simulations were validated against the benchmark results of Ghia et al. (1982) for Reynolds number of 100 and 400. The formulation of the test case and the results obtained from the simulations are explained in the sections to follow.

8.1.1 Formulation of the test case

Figure 8.1 shows the schematic diagram of the problem. The test case is a two-dimensional square cavity of unit length with a moving lid at the top and covered with walls on all the other three sides. *Re* for this internal recirculating flow is defined as follows:

$$Re = \frac{\rho v_{lid} d}{\mu} \tag{13}$$

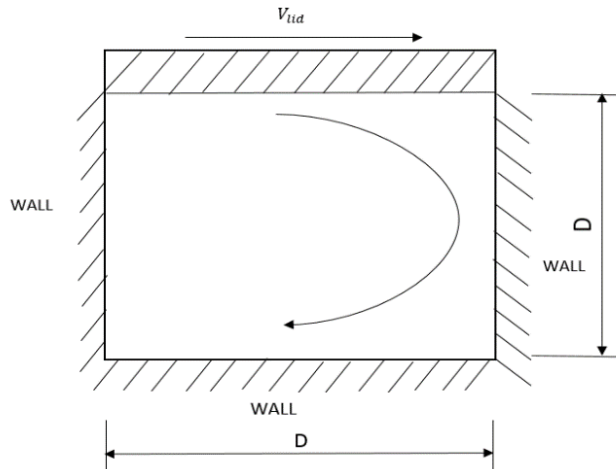Where v_{lid} is the velocity of the upper lid and d is denotes the length of the cavity.

Figure 8.1 – Schematic representation of Lid driven cavity.

50

8.1.2 Boundary Conditions

The initial condition is *u, v, and p* = 0 everywhere, and the boundary conditions are:

u = 1 at y = d (the "lid");

u, v = 0 on the other boundaries;

$\frac{\partial p}{\partial y} = 0$ at y = 0;

p = 0 at y = d

$\frac{\partial p}{\partial x} = 0$ at x = 0, d

8.1.3 Results and discussion

Grid independency studies are performed for $Re = 400$. It is observed that an accurate result is obtained for 150×150 grid than a 100×100 grid. The comparison of the and u velocity variation along the horizontal and vertical centreline of the cavity is shown in Figure 8.2 and Figure 8.3. With increase in grid resolution, the simulation took a large time to converge to a final steady state result.
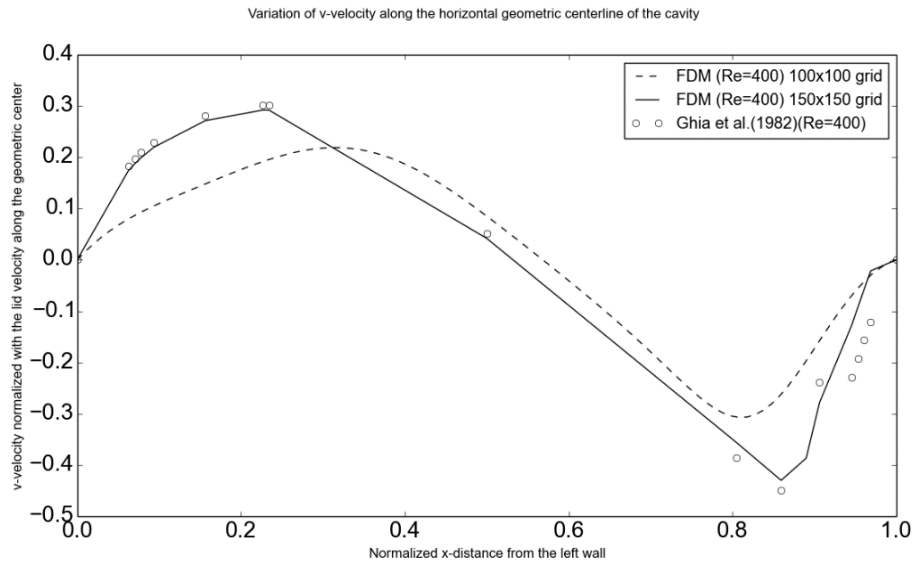
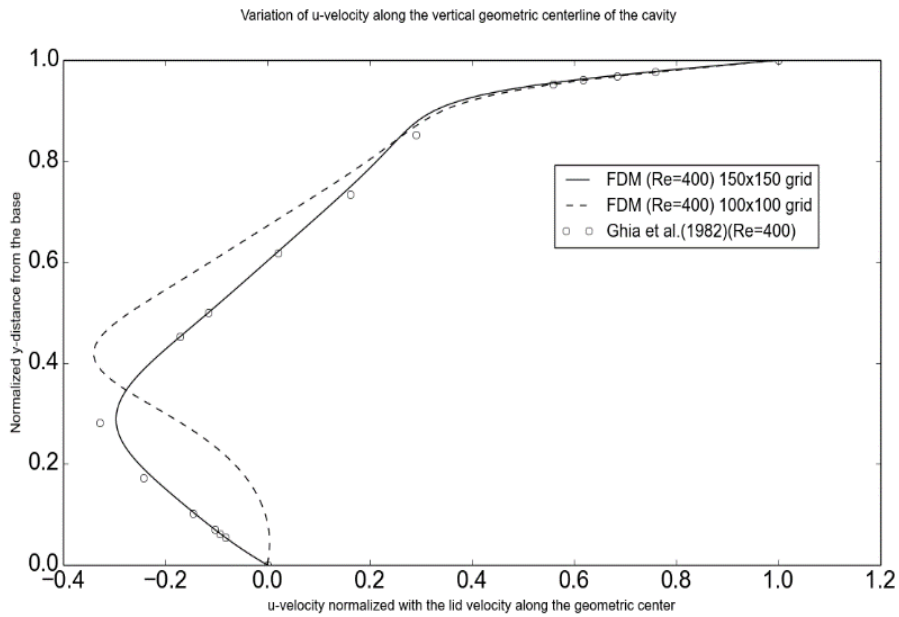Figure 8.2 - Variation of v-velocity along the horizontal geometric centreline of the cavity for Re = 400.

Figure 8.3 - Variation of u-velocity along the vertical geometric centreline of the cavity for $Re = 400$.

Cavity flows in simple geometries can become complex with increase in Reynolds number. Figure 8.4 shows a schematic representations of the flow structures in a lid driven cavity at high Re.
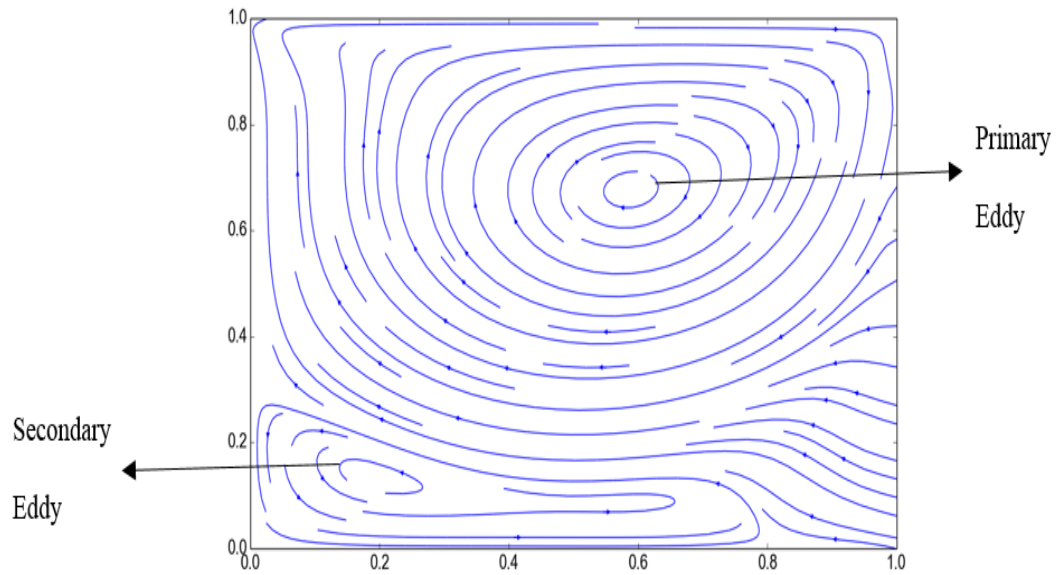

Figure 8.4 - Schematic diagram of flow structures in a lid driven cavity at higher *Re*.

The simulations were carried out with a 100*100 grid for *Re* = 100 and with 150*150 grid for *Re* = 400. The unsteady solver was run for a required number of time steps to obtain steady state results. The comparison of the u and v velocity variation along the vertical and horizontal centreline of the cavity respectively with the benchmark results for *Re* = 100 and *Re* = 400 are shown in Figure 8.5, 8.6, 8.7 and 8.8. For all results, the numerical results are in close agreement with the benchmark results of Ghia et al. (1982).
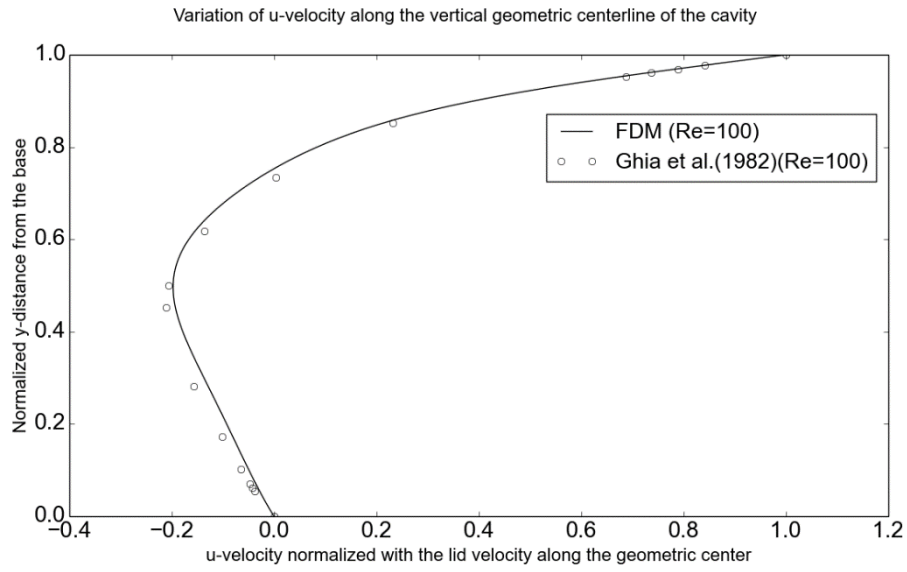
Variation of u-velocity along the vertical geometric centerline of the cavity

Figure 8.5 - Comparison of variation of u-velocity along the vertical geometric centreline of the cavity for *Re* =100.

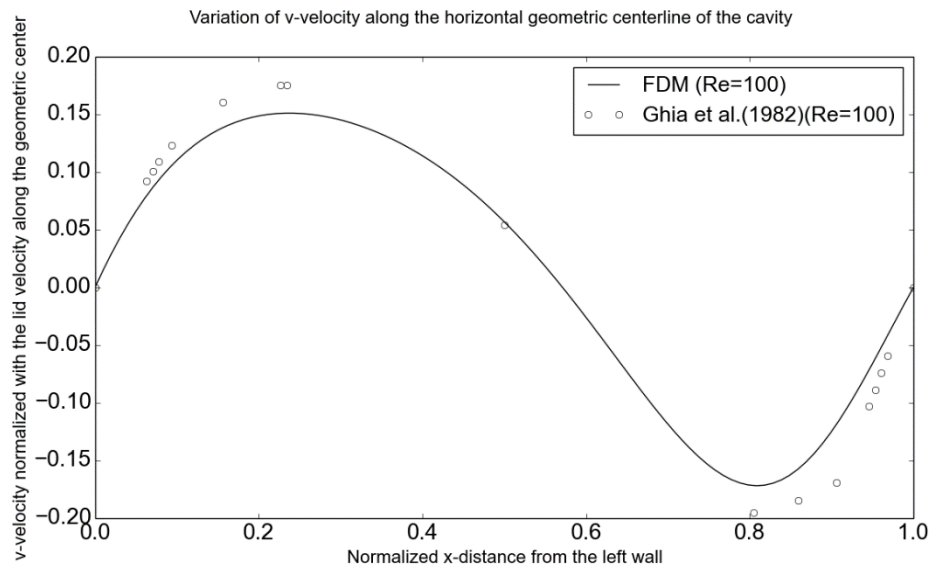Variation of v-velocity along the horizontal geometric centerline of the cavity

Figure 8.6 - Comparison of variation of v-velocity along the horizontal geometric centreline of the cavity for *Re* =100.
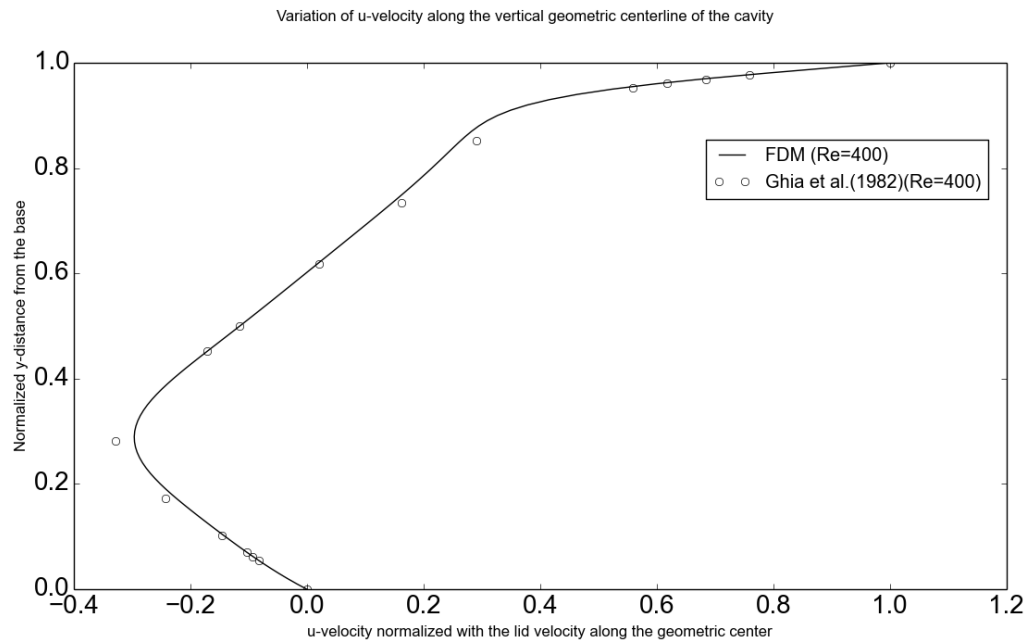
Figure 8.7- Comparison of variation of u-velocity along the vertical geometric centreline of the cavity for *Re* =400.
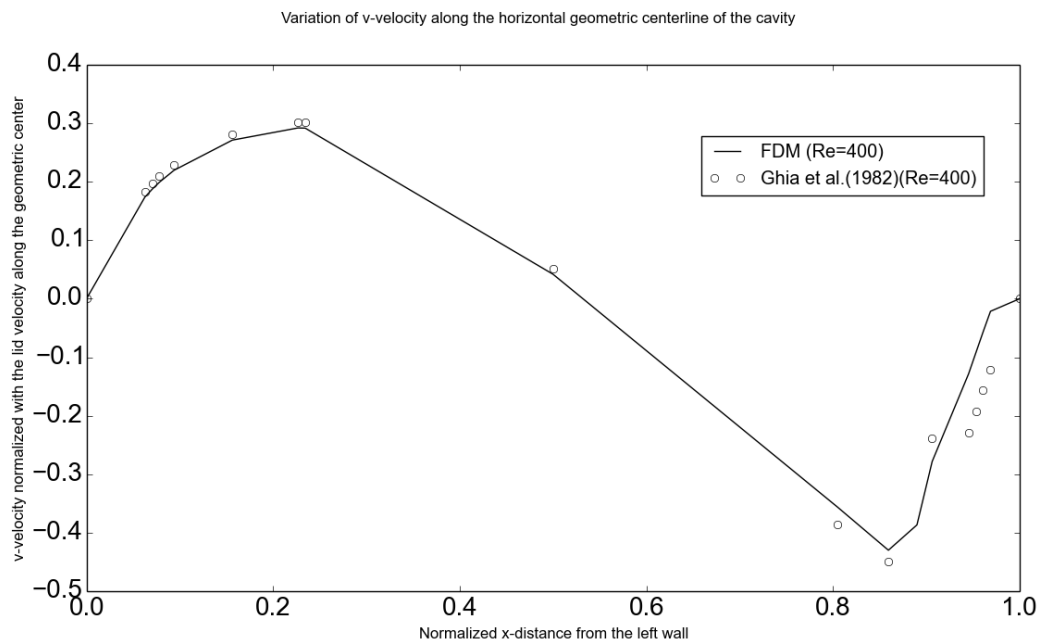

Figure 8.8 - Comparison of variation of v-velocity along the horizontal geometric centreline of the cavity for *Re* =400.

Figure 8.9 and 8.10 depicts the streamline plot within the cavity for $Re = 100$ and $Re = 400$, Figure 8.11 and 8.12 depicts velocity vector plot within the cavity for $Re = 100$ and $Re = 400$ and Figure 8.13 and 8.14 depicts pressure contour plot within the cavity for Re = 100 and Re = 400. Certain preliminary observations that can be made from the streamline plots are as follows. The width the of primary eddy increases with Reynolds number. Even for low Reynolds number of around 100, the velocity field loses its symmetry about the mid-plane. For $Re = 100$, the primary eddy is majorly free vortex in nature. With increases in Reynolds number there is a continuous evolution of eddies and the secondary eddies become bigger. For $Re = 400$, the eddy centre moves towards the centre of the cavity and the lower secondary eddies become bigger when compared with that of Re = 100.
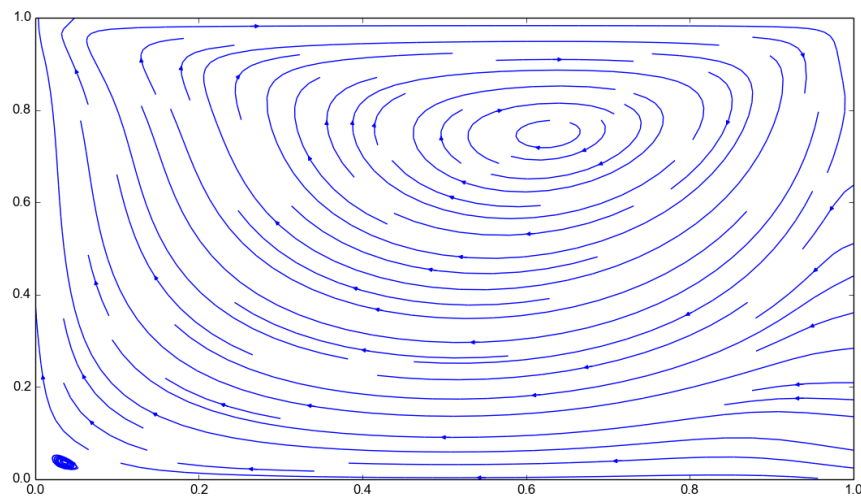

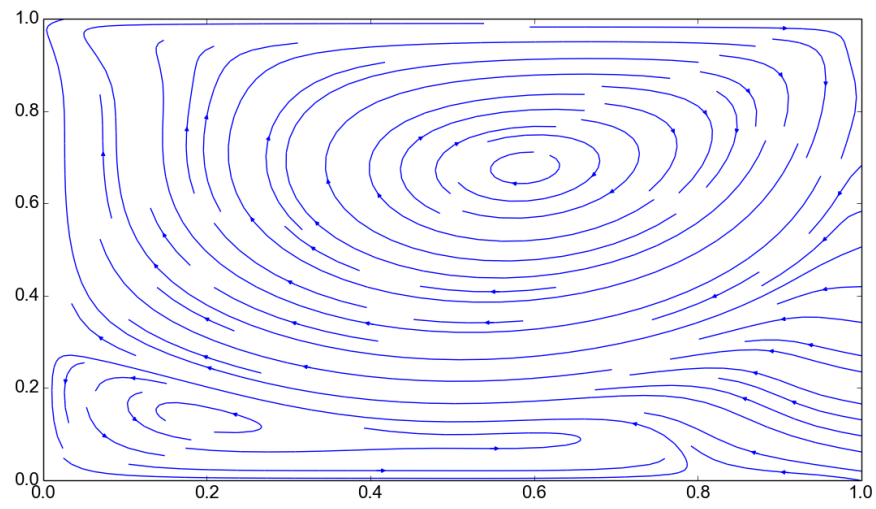Figure 8.9 - Streamline plot for $Re = 100$.

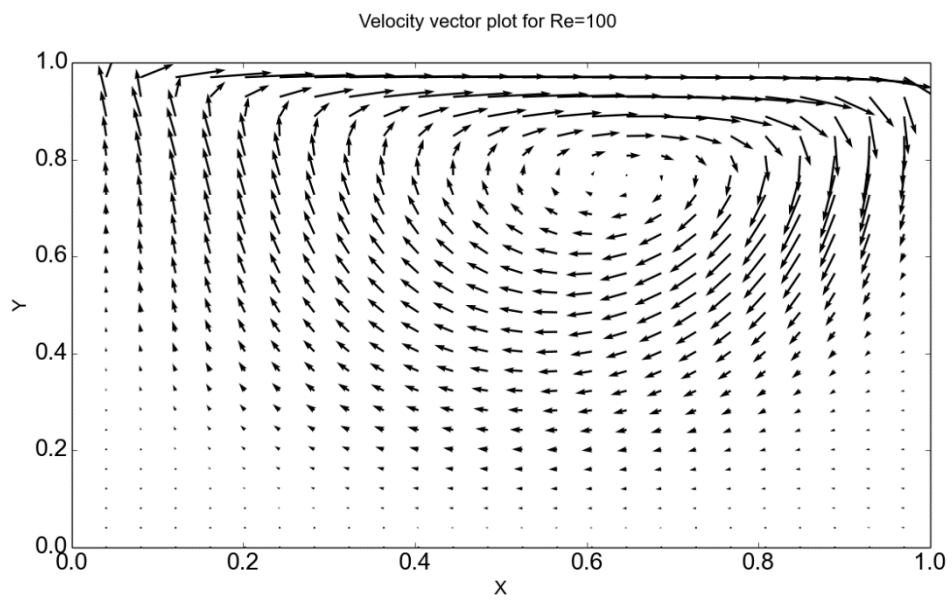Figure 8.10 - Streamline plot for $Re = 400$.

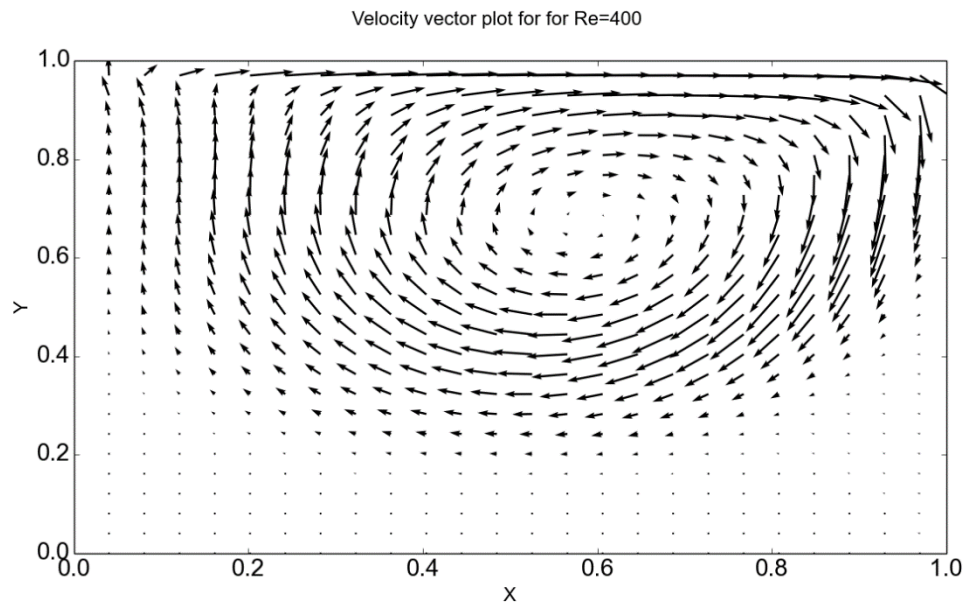Figure 8.11 - Velocity vector plot for $Re = 100$.
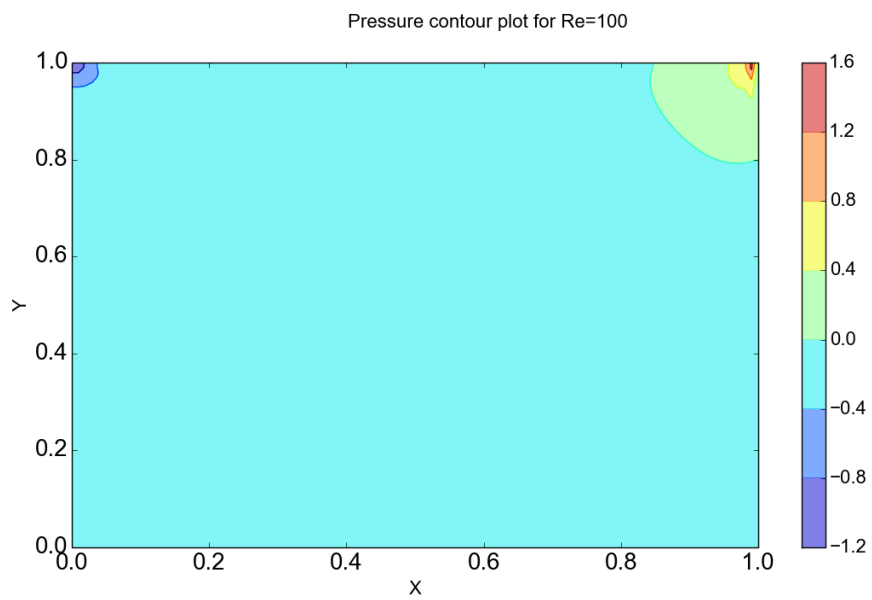
Figure 8.12 - Velocity vector plot for $Re = 400$.

Figure 8.13 - Pressure contour plot for $Re = 100$.
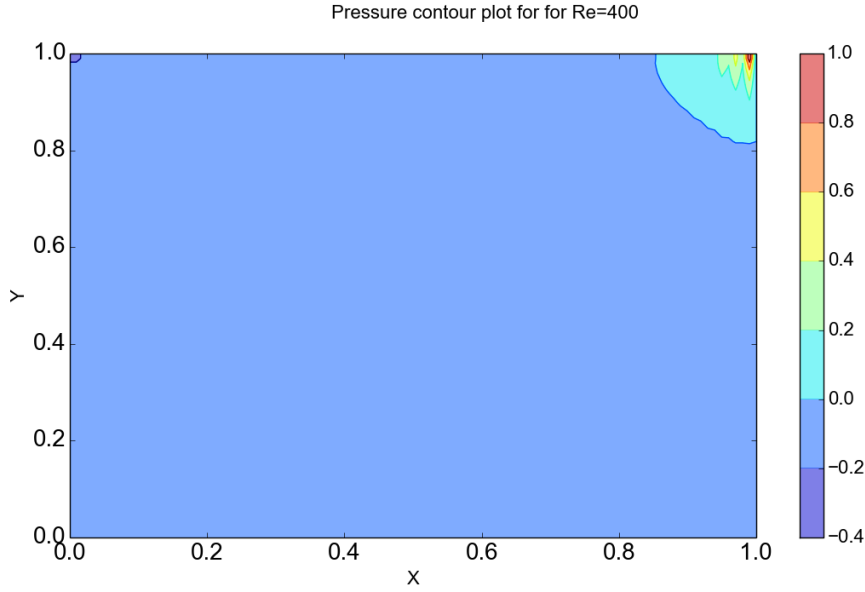
Figure 8.14 - Pressure contour plot for $Re = 400$.

8.2 Square Cylinder

Flow around a square cylinder in a channel gives a preliminary flow configuration of flow around bluff bodies. This was chosen to accommodate a Cartesian grid as the computational domain for the newly developed CFD solver. The flow is steady until $Re = 50$ and later the solution is periodic in nature. The formulation of the test case and the results obtained from the simulations are explained in the sections to follow.

8.2.1 Formulation of the test case

The test case consists of a solid two-dimensional square which is placed in a plane channel. The height and width of the plane channel are $8H$ and $40H$ respectively, where H is the characteristic dimension of the square cylinder. An entry length of $8H$ is kept to avoid the inlet flow disturbances and allow sufficient space for flow development. The cylinder is placed at the centre in cross stream direction. A domain

of $31H$ is kept in the wake to capture the flow disturbance downstream. The schematic

diagram of the domain is shown if Figure 8.15.
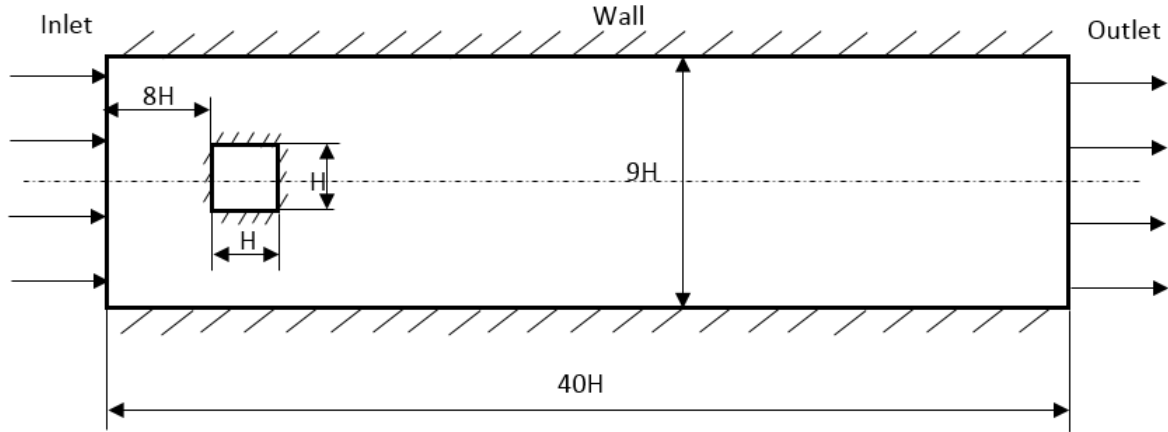
Figure 8.15 - Schematic diagram of flow around a square cylinder placed in a channel.

8.2.2 Boundary Conditions

The initial condition is *u, v, and p* = 0 everywhere, and the boundary

conditions are:

u = 1 at y = 0 (inlet);

u, v, p are periodic on x = 0, 40H;

$\frac{\partial p}{\partial y} = 0$ at y = 0, 9H;

u, v = 0 at y = 0, 9H;

Source term $F = -\frac{\partial p}{\partial x} = 1$ everywhere;

Cylinder boundary is set to wall boundary condition.

8.2.3 Results and discussion

Figure 8.16 and Figure 8.17 depict the streamline and pressure contour plot for $Re = 10$. The simulations were carried out with a 240×54 grid for $Re = 10$. The unsteady solver was run for a required number of time steps to obtain steady state results. There is a gradual development of wake vortex which is seen behind the cylinder in the streamline plot. The pressure contour plot as shown in Figure shows variation in pressure around the separated boundary layer from the upstream corners of the square cylinder feeding the primary vortex in the wake.
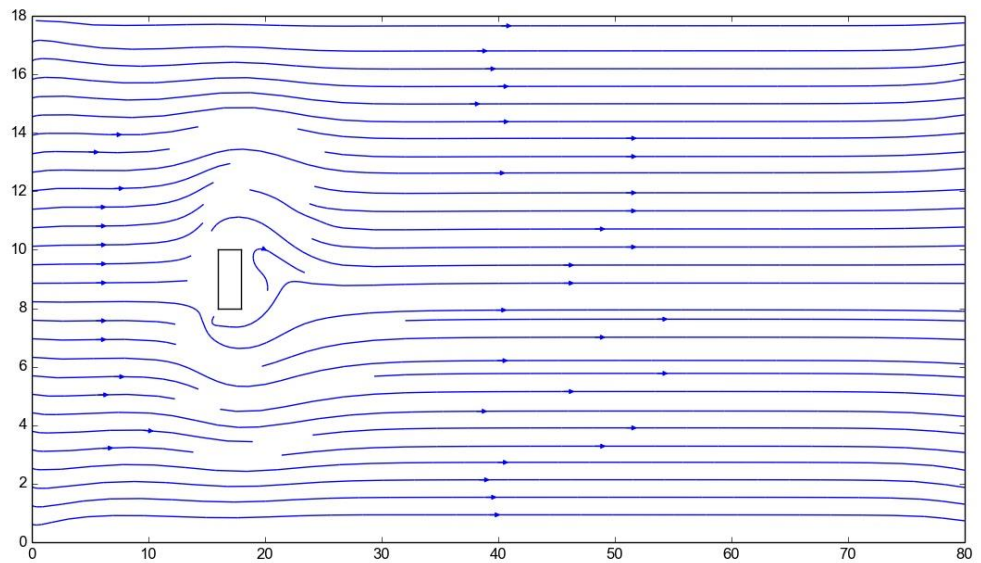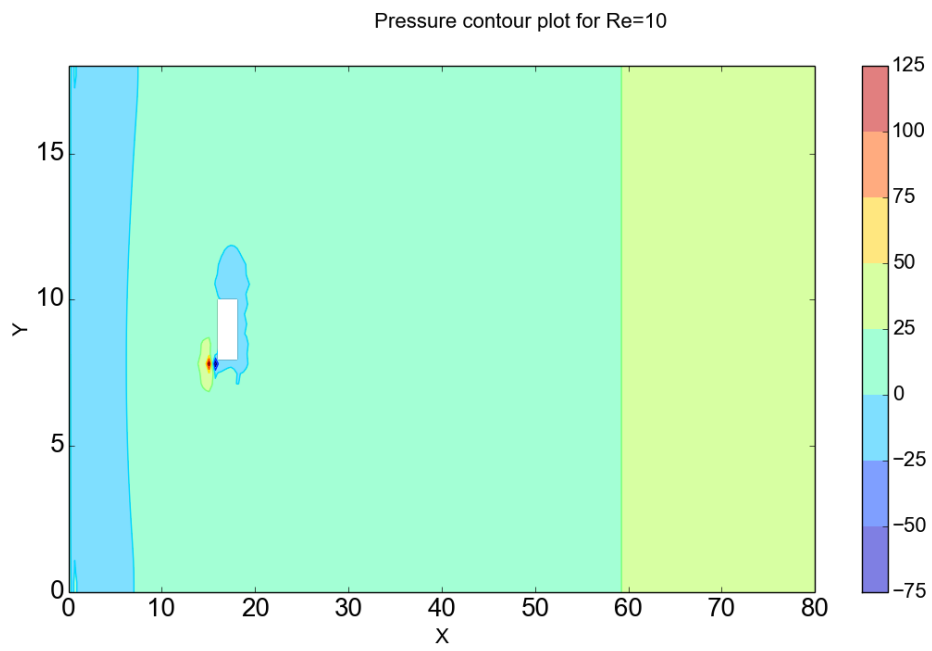
Figure 8.16 - Streamline plot for $Re = 10$.

Figure 8.17 - Pressure contour plot for $Re = 10$.

Chapter 9

Conclusions and future work

The experimental test section was designed and then was fabricated by assembling Perspex glass and supports were provided using angles made of mild steel. CPVC piping was used and the required range of Reynolds numbers was obtained by provision of valves. A $^1/_4$ HP pump was used to drive the flow. The experiment was carried out with a nylon cylinder of aspect ratio 12 as the specimen. The experiments were conducted for Reynolds number up to 300. Three sets of results were obtained and documented. Laminar flow at $Re = 46$, standing vortices at $Re = 155$ and vortex street at $Re = 255$. The experiments showed results that had good agreement with theoretical Reynolds number ranges. The theoretical ranges for the same being $10 < Re < 60$, $60 < Re < 140$ and $140 < Re < 50000$ respectively. The experiment also showed good repeatability upon multiple trials.

For future work the primary goal will be to make the system more versatile in terms of test specimens as well as range of Reynolds numbers. This can be implemented using a bigger test section with adjustable end plates to have variable channel width. A frequency controller can be installed in the pump to accurately adjust the output of the pump and to obtain a wider range of Reynolds number. The general stability of the system was not up to the mark as a few leaks were present. The leaks can be minimized by reducing the number of holes which are drilled on the test section. The leaks can also be mitigated using epoxy based sealants which would provide a long term solution. The table of the experimental setup can be provided with wheels to facilitate easy movement of the system. The system was crude in terms of data acquisition. Flow

meters or orifice meters can be implemented with the system during design phase which will help with the measurement of flow velocity. This will save a lot of time and will improve the accuracy of the results obtained. The cylinder can be graduated on the top surface to obtain the point of separation. The dye injection method adopted was very irregular and often didn't allow for good imaging. An automated system which provides constant flow of steady ink will be really useful to obtain continuous shots and will improve quality of results. Hydrogen bubble flow visualization technique can also be adopted for the same for improved flow visualization of unsteady and separated flows. The straw section can be replaced with a honeycomb section as a flow straightener as it would result in reduced flow losses.

References

1. Adrian, Ronald J. "Particle-imaging techniques for experimental fluid mechanics." Annual Review of Fluid Mechanics 23.1 (1991): 261-304.

2. Armfield, S. W. "Finite difference solutions of the Navier-Stokes equations on staggered and non-staggered grids." Computers & Fluids 20.1 (1991): 1-17.

3. Baranyi, László. "A finite difference method for flow past mechanically vibrated circular cylinders." (2000): 197-200. Hungarian Academy of Sciences.

4. Breuer, M., et al. "Accurate computations of the laminar flow past a square cylinder based on two different methods: lattice-Boltzmann and finite-volume." International Journal of Heat and Fluid Flow 21.2 (2000): 186-196.

5. Coe, Ryan. "Lid-Driven Cavity Flow using a Staggered Finite-Volume Pressure Correction Method." Virginia Tech Repository.

6. Ferziger, Joel H., and Milovan Peric. Computational methods for fluid dynamics. Springer Science & Business Media, 2012.

7. Fornberg, Bengt. "A numerical study of steady viscous flow past a circular cylinder." Journal of Fluid Mechanics 98.04 (1980): 819-855.

8. Gharib, Morteza, and Philip Derango. "A liquid film (soap film) tunnel to study two-dimensional laminar and turbulent shear flows." Physica D: Nonlinear Phenomena 37.1 (1989): 406-416.

9. Ghia, U. K. N. G., Kirti N. Ghia, and C. T. Shin. "High-Re solutions for incompressible flow using the Navier-Stokes equations and a multigrid method." Journal of Computational Physics 48.3 (1982): 387-411.

10. Goldstein, Sydney. "Fluid mechanics in the first half of this century." Annual Review of Fluid Mechanics 1.1 (1969): 1-29.

11. Gonçalves, R. T., et al. "Flow around circular cylinders with very low aspect ratio." Journal of Fluids and Structures 54 (2015): 122-141.

12. Govardhan, R., and C. H. K. Williamson. "Modes of vortex formation and frequency response of a freely vibrating cylinder." Journal of Fluid Mechanics 420 (2000): 85-130.

13. Grove, A. Shair, F. H. Shair, and E. E. Petersen. "An experimental investigation of the steady separated flow past a circular cylinder." Journal of Fluid Mechanics 19.01 (1964): 60-80.

14. Guilmineau, E., and P. Queutey. "A numerical simulation of vortex shedding from an oscillating circular cylinder." Journal of Fluids and Structures 16.6 (2002): 773-794.

15. Harlow, Francis H., and J. Eddie Welch. "Numerical calculation of time-dependent viscous incompressible flow of fluid with free surface." Physics of Fluids 8.12 (1965): 2182.

16. James, David F., and Allan J. Acosta. "The laminar flow of dilute polymer solutions around circular cylinders." Journal of Fluid Mechanics 42.02 (1970): 269-288.

17. Kundu, P. K., and L. M. Cohen. "Fluid Mechanics, 638 pp." Academic, Calif (1990).

18. Norberg, C. "An experimental investigation of the flow around a circular cylinder: influence of aspect ratio." Journal of Fluid Mechanics 258 (1994): 287-316.

19. Rajani, B. N., A. Kandasamy, and Sekhar Majumdar. "Numerical simulation of laminar flow past a circular cylinder." Applied Mathematical Modelling 33.3 (2009): 1228-1247.

20. Saffman, P. G., and J. C. Schatzman. "An inviscid model for the vortex-street wake." Journal of Fluid Mechanics 122 (1982): 467-486.

21. Shukla, Ratnesh K., and Jaywant H. Arakeri. "Minimum power consumption for drag reduction on a circular cylinder by tangential surface motion." Journal of Fluid Mechanics 715 (2013): 597-641.

22. Son, Jaime S., and Thomas J. Hanratty. "Numerical solution for the flow around a cylinder at Reynolds numbers of 40, 200 and 500." Journal of Fluid Mechanics 35.02 (1969): 369-386.

23. Sun, Lin, Sanjay R. Mathur, and Jayathi Y. Murthy. "An unstructured finite-volume method for incompressible flows with complex immersed boundaries." Numerical Heat Transfer, Part B: Fundamentals 58.4 (2010): 217-241.

24. Tritton, D_J. "Experiments on the flow past a circular cylinder at low Reynolds numbers." Journal of Fluid Mechanics 6.04 (1959): 547-567.

25. Versteeg, Henk Kaarle, and Weeratunge Malalasekera. An introduction to computational fluid dynamics: the finite volume method. Pearson Education, 2007.

26. Wesseling, P., A. Segal, and J. J. I. M. Kan. Finite volume discretization of the incompressible Navier-Stokes equations in general coordinates on staggered grids. Delft University of Technology, 1991.

27. Williamson, C. H. K. "Oblique and parallel modes of vortex shedding in the wake of a circular cylinder at low Reynolds numbers." Journal of Fluid Mechanics 206 (1989): 579-627.

28. Williamson, Charles HK. "Vortex dynamics in the cylinder wake." *Annual review of Fluid Mechanics* 28.1 (1996): 477-539.

29. Williamson, C. H. K., and R. Govardhan. "Vortex-induced vibrations." Annu. Rev. Fluid Mech. 36 (2004): 413-455.

Appendix A

The divergence of the momentum equation in the partial notation:

M is the vector of momentum equation.

The divergence is:

$$\nabla M = \frac{\partial}{\partial x} M_x + \frac{\partial}{\partial y} M_y$$

(14)

$$\frac{\partial}{\partial x} M_x = \frac{\partial}{\partial x}\frac{\partial u}{\partial t} + \frac{\partial u}{\partial x}\frac{\partial u}{\partial x} + u\frac{\partial^2 u}{\partial x^2} + \frac{\partial v}{\partial x}\frac{\partial u}{\partial y} + v\frac{\partial^2 u}{\partial x \partial y}$$

$$= -\frac{1}{\rho}\frac{\partial^2 p}{\partial x^2} + v\left(\frac{\partial^3 u}{\partial x^3} + \frac{\partial^3 u}{\partial x \partial y^2}\right)$$

(15)

$$\frac{\partial}{\partial y} M_y = \frac{\partial}{\partial y}\frac{\partial v}{\partial t} + \frac{\partial u}{\partial y}\frac{\partial v}{\partial x} + v\frac{\partial^2 v}{\partial y^2} + \frac{\partial v}{\partial y}\frac{\partial v}{\partial y} + u\frac{\partial^2 v}{\partial x \partial y}$$

$$= -\frac{1}{\rho}\frac{\partial^2 p}{\partial y^2} + v\left(\frac{\partial^3 v}{\partial y^3} + \frac{\partial^3 v}{\partial x^2 \partial y}\right)$$

(16)

Adding the LHS

$$\frac{\partial}{\partial x} M_x + \frac{\partial}{\partial y} M_y$$

$$= \frac{\partial}{\partial t}\left(\frac{\partial u}{\partial x} + \frac{\partial v}{\partial y}\right) + \left(\frac{\partial u}{\partial x}\right)^2 + \frac{\partial u}{\partial y}\frac{\partial v}{\partial x} + u\frac{\partial^2 u}{\partial x^2}$$

$$+ u\frac{\partial^2 v}{\partial x \partial y} + \frac{\partial v}{\partial x}\frac{\partial u}{\partial y} + \left(\frac{\partial v}{\partial y}\right)^2 + v\frac{\partial^2 u}{\partial x \partial y} + v\frac{\partial^2 v}{\partial y^2}$$

$$= RHS$$

(17)

69

Re-arranging

$$\frac{\partial}{\partial x}M_x + \frac{\partial}{\partial y}M_y$$

$$= \frac{\partial}{\partial t}\left(\frac{\partial u}{\partial x} + \frac{\partial v}{\partial y}\right) + \left(\frac{\partial u}{\partial x}\right)^2 + 2\frac{\partial u}{\partial y}\frac{\partial v}{\partial x}$$

$$+ u\frac{\partial}{\partial x}\left(\frac{\partial u}{\partial x} + \frac{\partial v}{\partial y}\right) + \left(\frac{\partial v}{\partial y}\right)^2 + v\frac{\partial}{\partial y}\left(\frac{\partial u}{\partial x} + \frac{\partial v}{\partial y}\right) \tag{18}$$

$$= RHS$$

Applying continuity, so $\nabla.u = 0$; Hence

$$\frac{\partial}{\partial x}M_x + \frac{\partial}{\partial y}M_y = \left(\frac{\partial u}{\partial x}\right)^2 + 2\frac{\partial u}{\partial y}\frac{\partial v}{\partial x} + \left(\frac{\partial v}{\partial y}\right)^2 = RHS \tag{19}$$

Adding the RHS

$$-\frac{1}{\rho}\left(\frac{\partial^2 p}{\partial x^2} + \frac{\partial^2 p}{\partial y^2}\right) + v\left(\frac{\partial^3 u}{\partial x^3} + \frac{\partial^3 u}{\partial x\partial y^2} + \frac{\partial^3 v}{\partial y^3} + \frac{\partial^3 v}{\partial x^2\partial y}\right) = LHS \tag{20}$$

Re-arranging

$$-\frac{1}{\rho}\left(\frac{\partial^2 p}{\partial x^2} + \frac{\partial^2 p}{\partial y^2}\right) + v\left(\frac{\partial^2}{\partial x^2}\left(\frac{\partial u}{\partial x} + \frac{\partial v}{\partial y}\right) + \frac{\partial^2}{\partial y^2}\left(\frac{\partial u}{\partial x} + \frac{\partial v}{\partial y}\right)\right) = LHS \tag{21}$$

Applying continuity, so $\nabla.\,\mathrm{u} = 0$; hence

$$-\frac{1}{\rho}\left(\frac{\partial^2 p}{\partial x^2} + \frac{\partial^2 p}{\partial y^2}\right) = LHS \tag{22}$$

Equating LHS & RHS

$$-\frac{1}{\rho}\left(\frac{\partial^2 p}{\partial x^2} + \frac{\partial^2 p}{\partial y^2}\right) = \left(\frac{\partial u}{\partial x}\right)^2 + 2\frac{\partial u}{\partial y}\frac{\partial v}{\partial x} + \left(\frac{\partial v}{\partial y}\right)^2 \tag{23}$$

The poisson equation in vector form

$$\nabla^2 p = -f \tag{24}$$

The poisson's equation in numerical domain.

Momentum equation for an incompressible fluid in vector form

$$\frac{\partial u}{\partial t} + u.\nabla u = -\frac{1}{\rho}\nabla p + v\nabla^2 u \tag{25}$$

Discretised momentum equation in vector form

Discretise in time: FD in time, with pressure at the n+1 (the pressure that correspond with velocity at n+1)

$$u^{n+1} = u^n + \Delta t\left(-u^n.\nabla u^n - \frac{1}{\rho}\nabla p^{n+1} + v\nabla^2 u^n\right) \tag{26}$$

The divergence of the momentum equation in vector form.

$$\nabla.u^{n+1} = \nabla.u^n$$

$$+ \Delta t\left(-\nabla.(u^n + \nabla.u^n) - \frac{1}{\rho}\nabla p^{n+1} + v\nabla^2.(\nabla.u^2)\right)$$

(27)

The poisson equation in vector form

The poisson equation for p at time n+1 and forcing $\nabla.u^{n+1} = 0$

$$\nabla^2 p^{n+1} = \rho\frac{\nabla.u^n}{\Delta t} - \rho\nabla.(u^n.\nabla u^n) + \mu\nabla^2(\nabla u^n)$$

(28)